Additive Manufacturing 61 (2023) 103319

Contents lists available at ScienceDirect

Additive Manufacturing

journal homepage: www.elsevier.com/locate/addma

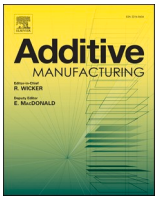

Research paper

High-cycle fatigue induced twinning in CoCrFeNi high-entropy alloy processed by laser powder bed fusion additive manufacturing

Yinan Chen [a], Bo Li [a,b,*], Bo Chen [c,**], Fuzhen Xuan [a,d]

[a] School of Mechanical and Power Engineering, East China University of Science and Technology, Shanghai 200237, China
[b] Additive Manufacturing and Intelligent Equipment Research Institute, East China University of Science and Technology, Shanghai 200237, China
[c] School of Engineering, University of Leicester, Leicester LE1 7RH, UK
[d] Shanghai Collaborative Innovation Center for High-end Equipment Reliability, Shanghai 200237, China

ARTICLE INFO

Keywords:
Fatigue
Twinning
Cellular structure
High-entropy alloy
Laser powder bed fusion

ABSTRACT

High-cycle fatigue (R=0.1, room temperature) induced microstructural evolution in a laser powder bed fusion (L-PBF) additively manufactured quaternary CoCrFeNi high-entropy alloy (HEA) was studied. The as-built material exhibited a combined < 001 > and < 110 > texture and high proportion of low-angle boundaries. Electron backscatter diffraction (EBSD) and transmission electron microscopy (TEM) revealed that deformation twinning occurred under the high-cycle fatigue of σ_{max}= 450 MPa (N_f=1.06 ×10^5), but not for the stress level o_f 300 MPa and 200 MPa. The deformation twins led to the cyclic softening, as manifested by the continuous increase of maximum strain under the stress-controlled fatigue, and the hardness increased by ~80 $HV_{0.2}$ in the post-fatigued condition. EBSD revealed that both the < 001 > and < 110 > orientations were favorable for the twin formation. Given that the size of grains with the < 001 > and < 110 > orientations was twice larger than those of the other orientations, the grain size effect on twin formation could play a certain role. High-resolution TEM revealed that the full dislocations, lattice distortion, stacking faults, and partial dislocations were associated with the twin, cellular and labyrinth wall-like dislocation structures. The underlying mechanism for the formation of nano-twins during high-stress fatigue involved the dissociation of 1/2 < 110 > full dislocations to 1/6 < 112 > partial ones. Moreover, the dislocation cell structure as observed in the as-built condition evolved into sub-grains after the high-cycle fatigue loading, with the immensely dense dislocations at the sub-grain boundary.

1. Introduction

Single-phase solid-solution alloys with a face-centered cubic (fcc) structure, composed of multiple principal elements in approximately equiatomic concentrations, are the most studied high-entropy alloys (HEA), e.g., the Cantor alloy CoCrFeMnNi. Compared to the extensive uniaxial tension/compression experiments (refer to a recent review article [1]), there are a few studies on fatigue behavior of the single-phase CoCrFeNi-based HEA, including those on fatigue crack growth [2–6], on low-cycle fatigue [7,8], and on high-cycle fatigue [9–12]. The aforementioned works can be divided into two groups, with one revealing the presence of deformation twins and favoring their beneficial effect on fatigue resistance [2–5,9,10,12], while the other reporting the absence of twins or little effect on fatigue [6–8,11]. Wang et al. [13] studied the twin boundary cracking behavior under low-cycle fatigue of the CoCrFeMnNi HEA with different grain sizes. It was found that with the increase of the difference in the Schmid factors between the matrix and twin, the damage mode transition occurred from slip band cracking to twin boundary cracking near the twin boundary regions. Their research finding implies that the smaller grain size facilitates twin boundary cracking, despite twin boundaries are more effective in resisting fatigue cracking than the high-angle grain boundaries.

The improved fatigue performance due to twinning has been primarily attributed to the twin boundaries (e.g. [4,9,10]), which not only act as a barrier to dislocation motion, but also provide local sites to accommodate more dislocations and facilitate dislocation emission from the crack tip. The latter further promotes strain hardening at the crack tip and crack blunting, ultimately leading to a reduced crack growth rate. For the work reporting little effect of twinning on fatigue of the

* Corresponding author at: School of Mechanical and Power Engineering, East China University of Science and Technology, Shanghai 200237, China.
** Corresponding author.
E-mail addresses: libo@ecust.edu.cn (B. Li), bo.chen@leicester.ac.uk (B. Chen).

https://doi.org/10.1016/j.addma.2022.103319
Received 11 July 2022; Received in revised form 23 October 2022; Accepted 23 November 2022
Available online 26 November 2022

HEA, the conclusions are only valid under certain material and test conditions. For example, Tian et al. [11] found that the fatigue performance of fine-grained CoCrFeMnNi HEA without the twin was better than that of coarse-grained counterpart with twins. Thurston et al. [6] found no evidence of twinning during fatigue-crack-growth tests at room temperature based on the fractography by scanning electron microscopy (SEM) as well as the orientation analysis via the electron backscatter diffraction (EBSD). Specifically, they studied the CoCrFeMnNi HEA specimens in the rapid crack propagation stage and found that the fatigue crack did not decelerate or deflect in the presence of deformation twin [6]. But, in another fatigue work [9], both the SEM and transmission electron microscopy (TEM) observations substantiated the presence of twins, leading Ghomsheh et al. [9] to conclude that high-cycle fatigue deformation occurs due to the combined interaction of planar slip and twinning. Given the discrepancy, further work is required to help elucidate under what circumstances can the fatigue-induced twinning occur in the single-phase CoCrFeNi-based HEA. In addition, there have been so much more research on the twinning of the CoCrFeNi-based HEAs during low-cycle fatigue and fatigue crack growth than the high-cycle fatigue.

Powder-bed fusion additive manufacturing (AM) is a fast-growing area of research interest as it enables the fabrication of complex-shaped components with reduced time and cost, whilst achieving improved or comparable mechanical properties thanks to the refined microstructure [14–16]. The good AM printability of the CoCrFeNi-based HEA has been demonstrated by different groups led by Pham [7], Lee [12], Kim [14], Li [17], Attalah [18], Zhou [19], Xuan [20], Yang [21], and Wei [22], to name a few. Their focus was placed mostly on the AM process parameters in relation to the as-built microstructure, defects, and monotonic properties, with the exception of the works reported in [7,12,22]. For example, Zhu et al. [22] elaborated how the dislocation cellular structure enhanced the tensile strength and confirmed the role of dislocation hardening rather than cellular boundary strengthening. Low-cycle fatigue of the CoCrFeMnNi HEA processed by laser powder bed fusion AM (L-PBF) was studied systematically in [7], where dislocation slip was found to be the dominant mechanism for cyclic plasticity, namely, the insignificant role of twinning. By contrast, the work performed on the L-PBF built HEA (L-PBF-HEA) with the same alloy type in [12] suggested that twinning is responsible for the enhancement of fatigue resistance. Thus, contradictory results exist regarding the role of fatigue-induced twinning in the single-phase CoCrFeNi-based L-PBF-HEA.

To summarize, there is limited work reporting the high-cycle fatigue behavior of the single-phase CoCrFeNi-based L-PBF-HEA and whether twinning can occur under low-stress amplitudes remains a question. The present work aims to fill in this knowledge gap for twofold reasons: first, high-cycle fatigue is known as an important property for the industrial application of CoCrFeNi-based L-PBF-HEA as a structural material; second, both the cellular dislocation microstructure and crystallographic texture related to the L-PBF process create opportunities to shed light on the correlations between initial microstructure and fatigue micro-mechanisms (i.e., twinning below the macroscopic yield) in fcc metals with low stacking-fault-energy (SFE) values of 18–45 mJ/m^2 [23].

In this paper, high-cycle fatigue behavior of the CoCrFeNi L-PBF-HEA is investigated over the life regime of 10^4 to 10^7 cycles. Prior to and post-fatigue microstructural analyses were performed using a range of complementary characterization tools with a particular emphasis on understanding the deformation twin formation in relation to the microstructure evolution. Thereafter the underlying mechanism responsible for the high-cycle fatigue of L-PBF-HEA is discussed. The quaternary 3d transition metal CoCrFeNi HEA has been chosen because it serves as an elementary base composition providing a platform for the HEA alloy design.

2. Material and experimental

By means of pre-alloyed powders produced by gas atomization, CoCrFeNi HEA samples were fabricated using L-PBF. Chemical composition of CoCrFeNi powders was measured using inductively coupled plasma atomic emission spectroscopy. Concentration of Co, Cr, Fe and Ni was 26.33, 22.86, 24.71 and 26.10 (all in wt%), respectively, with the corresponding atomic percent of 25.19, 24.79, 24.95 and 25.07. Oxygen content was analyzed by means of inert gas fusion and found to be below 200 ppm.

Fig. 1a shows the powder size distribution, obtained by using the laser particle diffraction method, and the particle size characteristics in terms of the D10, D50 and D90 were determined as 24.1, 36.3 and 58.6 μm, respectively. Fig. 1b reveals the spherical nature of the powder particle as well as some grooves delineating grain boundaries. SEM-based energy dispersive spectroscopy (EDS) elemental analysis confirms the homogeneity of the Co, Cr, Fe and Ni, Figs. 1c to 1f, respectively, for the as-processed powder condition.

A 316 L stainless steel starting plate was employed, and the L-PBF-HEA samples were built in an argon atmosphere with a purity level of 99.98%. Detailed information about the L-PBF machine and the laser source can be found in [16,20]. Sample coupons with the dimension of $6 \times 6 \times 6\ mm^3$ were produced using a range of L-PBF parameters, including laser power P of 250–325 W and scan speed v of 400–900 mm/s, whilst keeping the fixed values for the layer height (l=50 μm), hatch spacing (h=90 μm) and line offset of 0.09 mm. Based on the design-of-experiment, the optimal beam power and scan speed were identified as $P = 300$ W and v= 700 mm/s. The layer re-melting strategy with $P = 150$ W and v= 1000 mm/s was also employed to achieve better densification. Overall, a relative density of 99.5% (Archimedes drainage method) was achieved, and virtually no porosity or lack-of-fusion defect can be seen by optical microscopy. A unidirectional laser-beam scan strategy was used, as indicated by scanning direction (SD) in Fig. 1g, and no 90° beam rotation was applied between layers. Neither the contour nor shell was made. Both the fatigue and tensile specimens with a gauge length of 5 mm, a width of 13 mm, and a thickness of 3 mm were printed with their loading direction parallel to the transverse direction (TD), Fig. 1g. BD stands for the build direction. The concentration of C and N elements in the as-built sample was determined as 0.21 wt% and 0.15 wt%.

Prior to fatigue testing, specimen surfaces were ground down to 2000-grit SiC papers, and then subjected to polishing down to 2.5 μm diamond suspension, achieving a surface roughness with the Ra value of 0.2 as measured by using profilometer. Uniaxial stress-controlled fatigue testing (SUNS890 machine) was carried out at room temperature, with a stress ratio of R= 0.1, frequency of 20 Hz, under different maximum stress (σ_{max}) magnitudes from 475 MPa to 150 MPa to generate the stress vs. the number of cycles-to-failure (S-N) curves for the CoCrFeNi L-PBF-HEA. Fatigue run-out was defined as the 10^7 cycles without failure. The selected fatigue stress range was pre-defined according to the tensile test under a constant displacement rate of 0.01 mm/s, conducted on an Instron universal testing machine with a 100 kN load capacity. For both the tensile and high-cycle fatigue tests, no extensometer was attached due to the small sample dimension as well as the high-frequency loading. As a result, the strain was calculated from the crosshead displacement, and the effect of machine compliance was not accounted for due to the low load level (i.e., high-cycle fatigue). For the tensile test, the stress-strain curve was calculated by offset the elastic region. Micro-hardness measurements were conducted on selected specimens before and after the fatigue test.

A Tescan MIRA3 field-emission-gun scanning electron microscope (SEM) equipped with the backscattered electron (BSE) detector, energy-dispersive X-ray spectrometry (EDS), and electron backscatter diffraction (EBSD) detector was used for the microstructure and texture characterization. Metallographic sample preparation ended up with the colloidal silica suspension for polishing to achieve a nominal

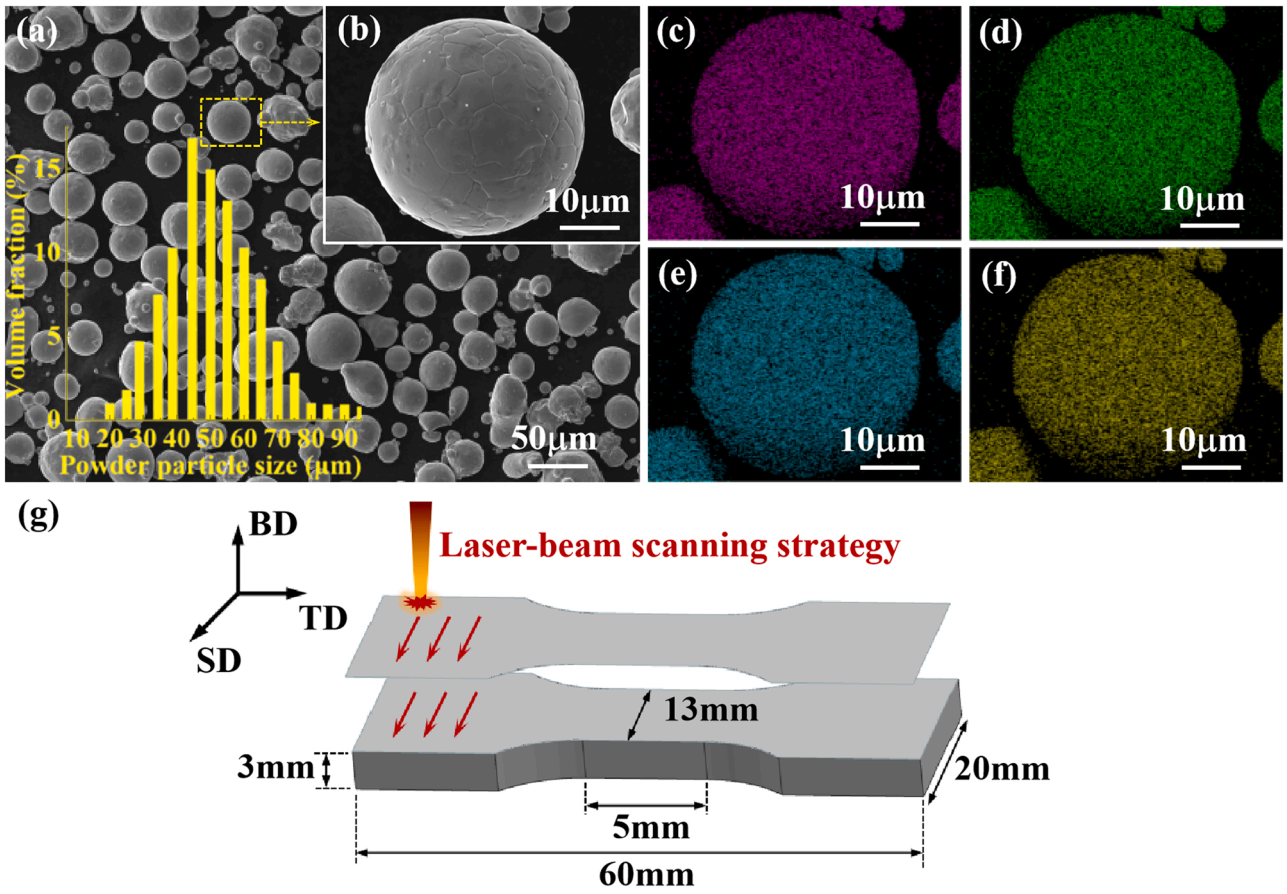

Fig. 1. Gas atomized HEA powder and L-PBF processing: (a) CoCrFeNi powder morphology and particle size distribution; (b) enlarged view of the powder; (c) to (f) EDS determined elemental distribution; (g) dimensions of tensile and fatigue specimens processed by L-PBF. Abbreviations of BD, SD, and TD stand for building direction, laser-beam scanning direction, and transverse direction of the L-PBF process, respectively.

deformation-free surface. To reveal the micro-melt pool microstructure, samples were electrolytically etched in a 10% oxalic acid solution. SEM fractography was used to identify the fatigue crack initiation and propagation characteristics.

EBSD scans were made with two different step sizes of 0.6 μm and 0.15 μm, depending on the length-scale of the feature of interest. Grain size and morphology, inverse pole figure (IPF) orientation maps and pole figures, grain boundary misorientation distribution (cut-off misorientation angle of >10° [24,25] for the high-angle grain boundaries, HAGBs), and the map of geometrically necessary dislocations (GND) were derived from the EBSD data using AZtecCrystal software package with the Burgers vector of b= 0.2518 nm [26,27]. A detailed description of the EBSD data post-processing can be found in [28].

To reveal the deformation twin and dislocation structures, a Talos F200X field-emission analytical transmission electron microscopy (TEM) operating at 200 kV was used for imaging and selected area diffraction (SAD). High-angle annular dark-field (HAADF) detector was used for the atomic-scale characterization in STEM mode. TEM samples were cut from the gauge section of post-fatigue specimens. Two fatigue conditions were investigated, with one tested at the higher stress of σ_{max}= 450 MPa, while the other tested under the much lower stress of σ_{max}= 200 MPa. TEM thin foil sample preparation involved mechanical polishing down to 0.5 mm thick and then further thinned with the ion beam using PIPS II, Gatan 695. Data post-processing was conducted using Digital Micrograph software. More details about the TEM sample preparation and TEM data processing can be found in [29]. All the microstructure observations for the post-fatigued samples were made on the TD-SD plane. The metallography samples were taken from the region within 1.5 mm from the fracture surface; this applies to both the TEM and EBSD samples.

3. Results and discussion

3.1. As-built microstructure

Fig. 2 shows the microstructure of the BD-TD cross-section of the CoCrFeNi L-PBF-HEA. Good process stability can be manifested by the uniformity and orderliness of the micro-melt pools. Within the micro-melt pool, the microstructure is characterized by the cellular structure, whose dimension ranges from several hundreds of nanometers to one micrometer in diameter or width for the elongated shape. Such cellular structure has been frequently observed in various alloys fabricated by L-PBF [25,30]. Despite contrasting viewpoints about its origin, the cellular structure is known to be metastable, associated with the rapid solidification process. There has been evidence to suggest the micro-segregation in the cell walls (e.g. [7,17,31]). The SEM images in Fig. 2 were taken from the sample that had been subjected to electrochemical etching in a 10% oxalic acid. Thus, the identified cell walls due to the preferential etching effect suggest the compositional difference. However, the SEM-based EDS analysis confirmed the homogeneous distribution of Co, Cr, Fe and Ni in the present L-PBF-HEA sample, whilst the X-ray diffraction measurement verified the monophase with fcc crystal structure (see Fig. S1 and S2 in Supplementary Material).

The cellular structures grew in different directions, Fig. 2b, illustrating two distinctive shapes: one is characterized by the near-equiaxed shape, while the other is columnar; for both types, no evidence suggesting secondary dendrite arms. There is no measurable size difference between the two by comparing the width of the columnar cells with the

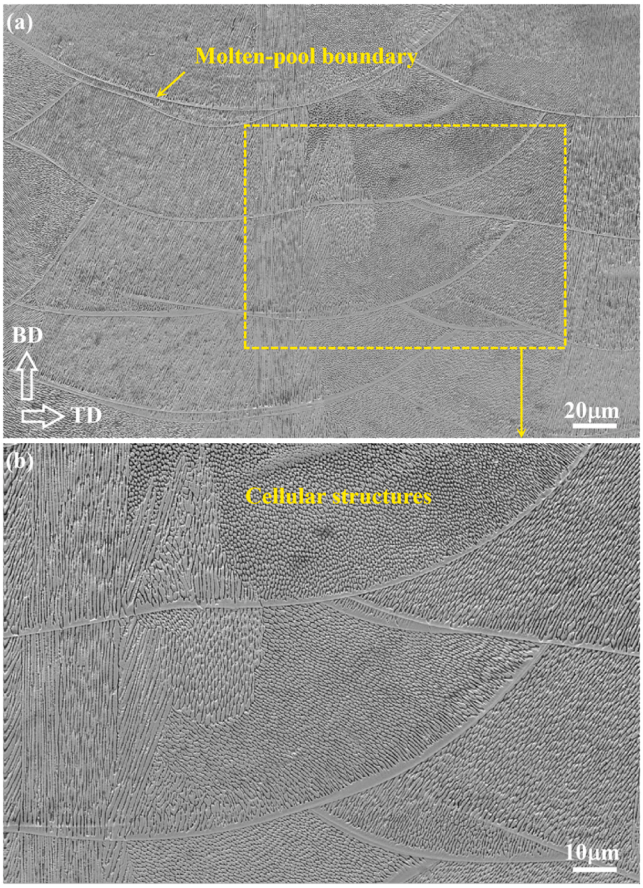

Fig. 2. L-PBF-HEA alloy microstructure revealed by SEM secondary electron imaging mode: (a) low magnification and (b) enlarged view showing the cellular structure. Sample preparation involved polishing and electrochemical etching in 10% oxalic acid solution.

diameter of the near-equiaxed ones. Such an SEM observation is as expected due to the fact that both the columnar and near-equiaxed cells are essentially the same. Note that a cross section is the 2D shape obtained when a plane cuts a 3D solid. Fig. 3 shows the TEM images of the CoCrFeNi L-PBF-HEA in the as-built condition. It can be seen that the dislocation cellular structure was developed, Fig. 3a, exhibiting a clear difference in dislocation density between the region close to the cell walls and the cell interior, Fig. 3c. The higher magnification TEM image (bright-field in Fig. 3d while dark-field in Fig. 3e) reveals that those dislocations close to the cell walls were loosely tangled, and yet to form a well defined sub-grain boundary. Finally, the SAD pattern in Fig. 3b confirms the nature of monophase with a fcc structure.

Fig. 4 compiles a list of EBSD results obtained from the as-built CoCrFeNi L-PBF-HEA. The pseudo-3D view of IPF-BD maps, as shown in Fig. 4a, provides the overall information about the epitaxial grain growth. For the BD-SD plane, $< 001 >$ orientation appears to be the dominant one and the average grain size was measured to be 30.57 μm (Fig. 4f). Majority of the grains are characterized by the columnar shape, with the longitudinal dimension being much larger than the layer height of 50 μm. This is as expected, given that $< 001 >$ direction is the easy growth direction for an fcc material and the maximum thermal gradient aligned towards the BD and SD directions of L-PBF samples, under the condition of no 90° rotation between the layers [12,32]. Wang et al. [30] studied the effect of the laser-beam scanning angle on the grain growth rate, and they suggested that at the top of the molten pool, dendrites followed the laser scanning direction and transition to the direction of maximum heat flow.

In terms of the SD-TD plane (Fig. 4d), both the $< 001 >$ and $< 110 >$ crystallographic orientations are the preferred ones, with the grain size determined to be 16.12 μm. The maximum intensities in multiples of the uniform density (MUD) at $< 001 >$ and $< 110 >$ orientations were measured to be 8.75 and 4.94, respectively (Fig. 4c). This suggests that the $< 110 >$ texture should not be ignored when assessing the as-printed microstructure. Fine grains of less than 10 μm in size but with over 60% in volume fraction were observed at the overlapping boundaries of laser tracks (Fig. 4d). The IPF-BD map taken from the TD-BD plane (Fig. 4e) reveals far less defined texture information when compared to the other two cross-sections. This could be attributed to the large grain size of 41.86 μm, which unfortunately limits the statistical rigor of the EBSD analysis.

The reason for the presence of combined $< 001 >$ and $< 110 >$ texture (Figs. 4c and 4d) can be explained by the dynamic scanning behavior of the laser beam, as depicted by the schematic diagram of Fig. S3 (Supplementary Material). When the laser beam moves along the horizontal direction (i.e., SD direction), the molten pool solidifies at the rear of the laser track under a large thermal gradient in the $< 100 >$ grain growth orientation along the SD. There is a maximum thermal gradient along the BD, which is parallel to the $< 001 >$ orientation. As a result, a portion of the grains would grow in a $< 110 >$ orientation along the direction between these two major thermal gradients. Zhou et al. [33] studied the effect of the laser-beam path, during the L-PBF process, on the orientation of CoCrMo alloy, and they found that columnar grains underwent complex heating cycles by the laser-beam scanning. This can cause the grain formation with the $< 110 >$ orientation and other orientations between the $< 110 >$ and $< 001 >$. In addition, Kim et al. [34] also found the phenomenon of $< 110 >$ orientation in the TD-SD plane in CoCrFeMnNi L-PBF-HEA. The Marangoni flow can affect the growth orientation of grains by changing the heat flow direction.

Fig. 4b presents the misorientation distribution histogram of the SD-TD plane, where the correlated misorientation calculation based on the neighboring data points exhibited a significantly high proportion of low-angle grain boundaries (LAGBs), with reference to the uncorrelated one as calculated using randomly chosen points. This suggests that numerous metastable sub-grain boundaries formed during the non-equilibrium solidification. This observation is consistent with the cellular structure as revealed by SEM imaging in Fig. 2 and TEM imaging in Fig. 3. The proportion of LAGBs on the SD-TD, TD-BD and SD-BD was found to be 55.0%, 71.4% and 57.3% (Fig. S4 in Supplementary Material), respectively, all suggesting the formation of sub-grains or dislocation cells in as-built CoCrFeNi L-PBF-HEA.

Figs. 4g to 4i illustrates the GND map for the three orthogonal planes, where the region of higher GND density corresponds to grain boundaries. The maximum GND value was found to be $19.02 \times 10^{14}/m^2$, which is higher than those of the homogenized HEA counterpart ($6.34 \times 10^{13}/m^2$ [10]) fabricated by conventional means. The non-equilibrium solidification, caused by the rapid melting and cooling of L-PBF process, triggers the development of metastable substructures and lattice defects in the as-printed condition [34,35]. The chaotic state of multi-principal elements in the HEA further hinders the stable arrangement of the lattice during the solidification [36].

3.2. Monotonic mechanical properties

Tensile properties of the CoCrFeNi L-PBF-HEA were measured to be 535 MPa for yield strength (σ_s), 601 MPa for ultimate tensile strength (σ_b), and ~30% for the elongation to failure, Fig. 5. The Young's modulus of the CoCrFeNi L-PBF-HEA was tested as ~169 GPa. The micro-hardness ($HV_{0.2}$) was determined as 189 ± 6.7 for the SD-TD plane, 187 ± 4.2 for the TD-BD plane, and 196 ± 4.4 for the SD-BD plane. Fig. 6 compares the average grain size, yield strength, and tensile ductility of the CoCrFeNi and CoCrFeMnNi HEAs fabricated by using conventional and AM methods. The data is a collection of a number of studies which have been carefully chosen, see Table 1. Both the yield

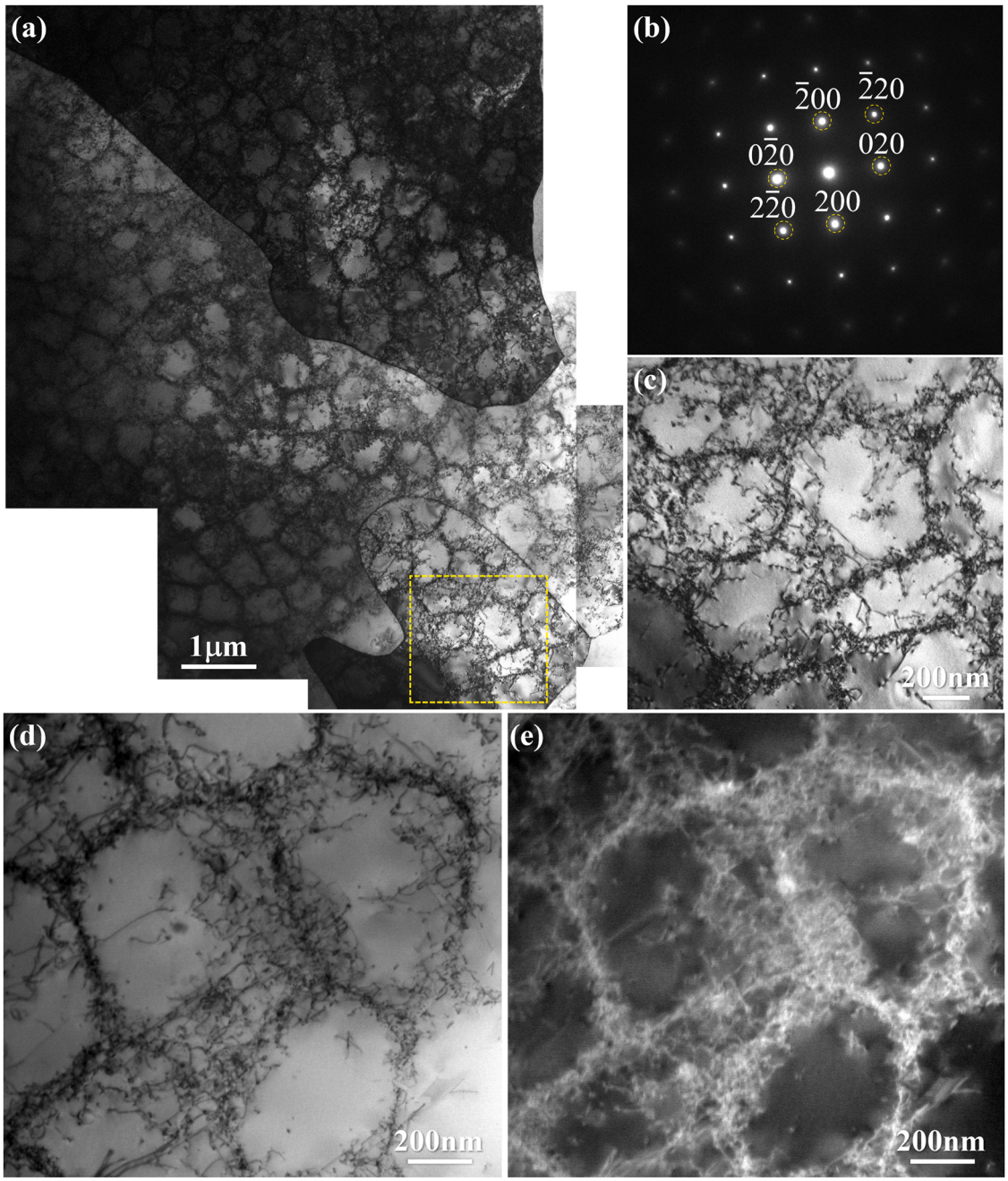

Fig. 3. L-PBF-HEA alloy microstructure revealed by TEM: (a) a low magnification image showing the cellular structure; (b) a selected area diffraction (SAD) pattern confirming monophase with the fcc crystal structure; (c) an enlarged view of the yellow outlined region in (a); (d) a bright-field image of the cellular structure; and (e) a dark-field image of the cellular structure.

strength (Fig. 6a) and ductility (Fig. 6b) of the present CoCrFeNi L-PBF-HEA are as good as the previous AM work. Moreover, compared to the conventional means, all the CoCrFeNi-based HEAs processed by AM exhibit a higher strength but a lower ductility, together with the generally finer grain size. Even with the similar grain size, the CoCrFeNi-based L-PBF-HEAs often show a higher tensile strength when compared to those produced by conventional means (i.e., vacuum induction melting [10,37] and arc melting [9,11]. The observed higher strength of the L-PBF-HEAs can be attributed to the fine grains and sub-micron dislocation cellular structures as observed in the present TEM observation (Fig. 3) and previous work [22,24,31]. It is generally recognized that the dislocation cell walls of the cellular structure can trap a high density of dislocations during deformation and store them inside the cells.

3.3. High-cycle fatigue

Fig. 7a displays the high-cycle fatigue S-N curve of the CoCrFeNi L-PBF-HEA, under R= 0.1 and at room temperature. The fatigue strength, determined by the run-out point at 10^7 cycles, is 170 MPa under the stress ratio of (R=0.1). Strictly speaking, "fatigue strength" is the stress corresponding to a certain fatigue life at stress ratio of R= −1 (pull-push fatigue). Given the stress ratio effect on fatigue strength, it is not accurate to use this phrase without specifying the condition of R= 0.1. Overall, fatigue data follows a double logarithmic relationship between σ_{max} and N_f, Fig. 7a, from which the fatigue strength coefficient (σ_f at R=0.1) was calculated as 11,694 MPa whilst the fatigue strength exponent (b at R=0.1) was determined to be − 0.29, according to the σ_{max}-N_f relationship. Three fatigue tests were conducted at

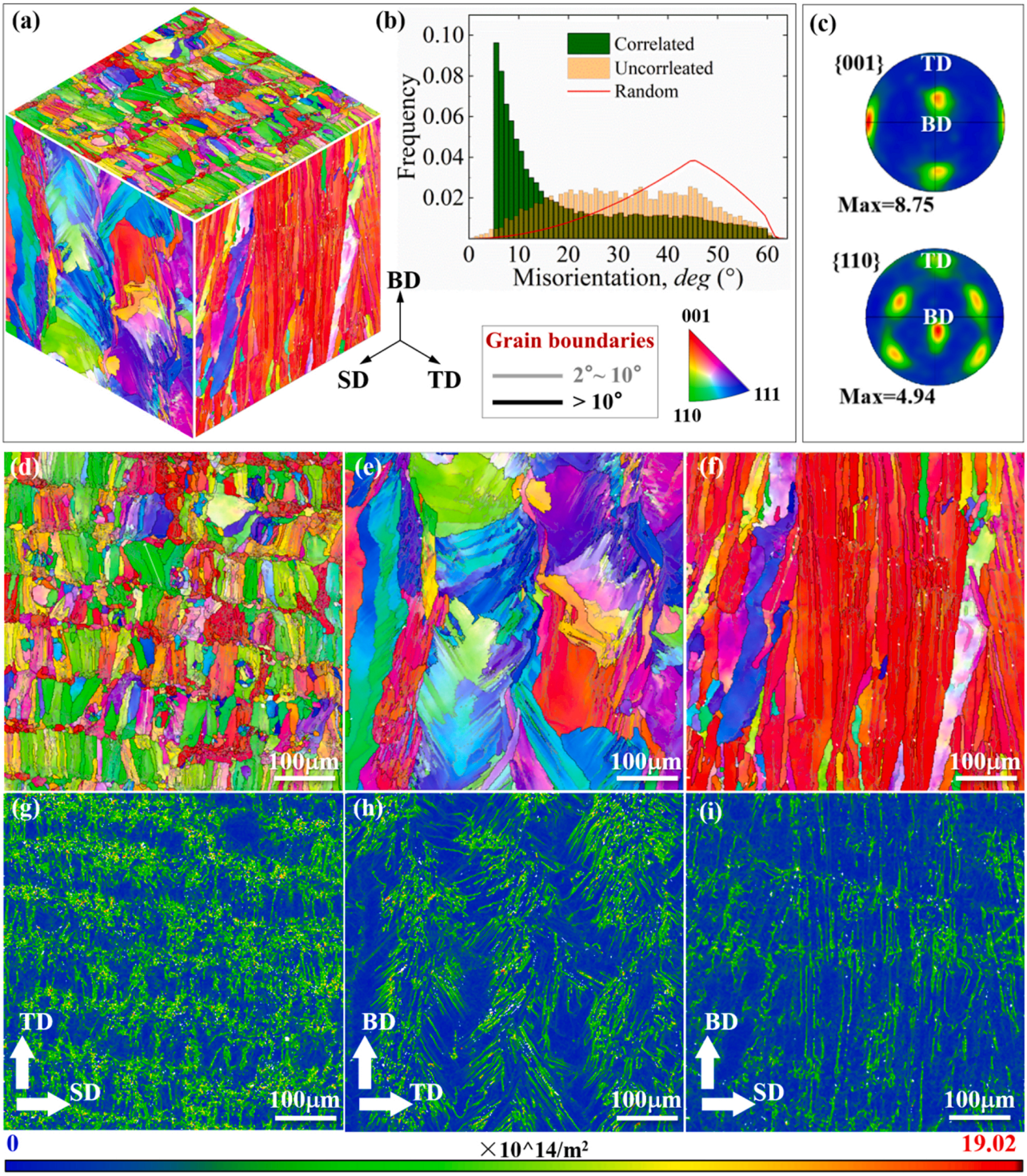

Fig. 4. L-PBF-HEA alloy microstructure in as-built condition as revealed by EBSD: (a) pseudo-3D view of the inverse-pole-figure (IPF) maps; (b) and (c) misorientation distribution plot and pole figures of the TD-SD cross-section, respectively; (d) to (f) IPF maps for the SD-TD, BD-TD and BD-SD, respectively; (g) to (i) geometrically necessary dislocations (GND) map for the three cross-sectional planes. The reference axis for all the IPF maps is parallel to the BD.

σ_{max}= 200 MPa, and the observed fatigue life scatter was reasonable, being 3.7×10^5, 3.0×10^5, and 7.4×10^5, respectively.

Fig. 7b shows the evolution of maximum strain as a function of fatigue cycles, under the test condition of σ_{max}= 450 MPa. The measured strain came from the displacement between the two clamping ends, and it represents the accumulative total strain. With the increase in fatigue cycles, the CoCrFeNi L-PBF-HEA exhibited a cyclic softening behavior, as manifested by the monotonically increasing levels of the maximum strain. Close to the fatigue failure cycle, a big jump in the maximum strain level is seen in Fig. 7b, probably caused by the event where the length of fatal fatigue crack triggered the final instantaneous failure.

Fig. 8a shows the overview fracture surface of the failed specimen tested at σ_{max}= 300 MPa, which is representative of all specimens considered in the present work. The fatal fatigue crack was triggered by the micropores at the near-surface location. The presence of micropores can also be seen in the interior of the specimen, but their volume fraction

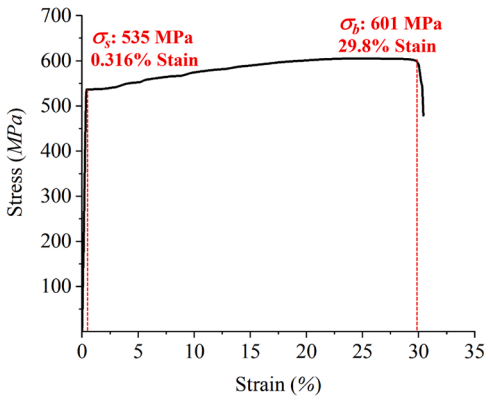

Fig. 5. Monotonic tensile stress-strain curve of CoCrFeNi L-PBF-HEA (the tensile direction was parallel to TD, as sketched in Fig. 1g).

was confirmed to be low and size was small based on the cross-section examination. Neither the unmelted powder nor partially melted one was found inside the micropore. Some of the micropores were quite large in size, but they were not continuous. It is thus believed that there is no lack-of-fusion defect in the present CoCrFeNi L-PBF-HEA.

Given the relative density of 99.5% (as measured in the bulk sample) achieved through the process optimization, the SEM fractography results suggest that it is challenging to entirely avoid the micropores. Kim et al. [12] found that the high-cycle fatigue life of the CoCrFeMnNi L-PBF-HEA was 20 times lower in the specimen having the near-surface defect, despite both specimens had a similar relative density. The formation of the micropores can be related to the following three reasons: first, during the laser-induced melt process, the violently tumbling molten pool inhales ambient gas above it due to the negative pressure effect [45,46]; second, during the rapid solidification, the time is not sufficient to allow the incoming gas escaped [45,47]; third, the voids in the powder bed induced by the quality of the powder size distribution [45,48].

High-magnification SEM fractography taken from the fatigue-crack propagation region, Fig. 8b and 8c (σ_{max}=300 MPa), reveals a typical feature of fatigue striations with their average spacing measured to be 0.68 μm. By comparison, the striation spacing was determined as 1.45 μm for the test condition of σ_{max}= 450 MPa (Fig. 8e), and 0.40 μm for the test performed at σ_{max}= 200 MPa (Fig. 8d). The higher fatigue load leads to wider striation spacing which is as expected.

Fig. 8f and 8g show the EBSD analysis on the BD-TD plane close to the fracture surface, with GND map shown in the former while IPF-BD orientation map (LAGBs defined by the less than 10° angle, delineated by grey lines) in the latter. The high GND-value regions correspond to the fracture surface as well as the sub-grain and grain boundaries. The proportion of the LAGBs reached 70.1%, which is higher than the as-built condition (55.0% in Fig. 4b). Also, just beneath the fracture surface, ultra-fine grains can be seen in Fig. 8g, which was most likely caused by the dynamic recrystallization [28,49]. Collectively, the results suggest that localized plasticity develops during high-cycle fatigue. Although the materials with low SFE are difficult to form LAGBs, the repeated rapid melting and non-equilibrium solidification of the L-PBF process triggers the formation of dislocation cellular structures with the metastable state (Figs. 3e and 3f). Voisin et al. [25] also found a high fraction (~50%) of LAGBs in the as-built condition of L-PBF 316 L stainless steel which is known to have a low SFE value.

Micro-hardness measurement was performed on both the σ_{max}= 200 MPa and 450 MPa specimens close to the fracture surface. Compared to the as-built condition (189 ± 6.7 $HV_{0.2}$), the micro-hardness for the σ_{max}= 200 MPa specimen increased slightly to 210 ± 10.1 $HV_{0.2}$, while that for σ_{max}= 450 MPa specimen increased vastly to 268 ± 7.7 $HV_{0.2}$. Therefore, it is believed that localized cyclic plasticity can certainly occur in the CoCrFeNi L-PBF-HEA during high-cycle fatigue.

3.4. *Twinning and dislocation sub-structure evolution induced by high-cycle fatigue*

Based on the EBSD results, there is evidence for twinning in the post-fatigued specimen tested at σ_{max}= 450 MPa, as indicated by regions A and B in Fig. 9a and their enlarged views in Fig. 10. The identification of twins was based on the coincidence site lattice (CSL) distribution maps; refer to Fig. S5b and S5c (Supplementary Material). By contrast, no evidence indicates twinning in the specimen tested at σ_{max}= 200 MPa. Hereafter, the fatigue specimen tested at σ_{max}= 450 MPa is referred to as *high stress*, while that tested at σ_{max}= 200 MPa is referred to as *low stress*, for convenience of description. EBSD samples for both the high-stress and low-stress conditions were extracted from the region within 1.5 mm distance to the fracture surface.

For the high-stress condition, two types of twinning are observed; one is characterized by the thickness of up to 1 μm (micro-twins, Fig. 10), while the other has the thickness of less than 100 nm (nano-twins, Fig. 10). The latter should be more precisely phrased as the 'micro-twins' which is a packet of multiple nano-twins (later confirmed using TEM in Fig. 13). Majority of those twins are parallel to each other

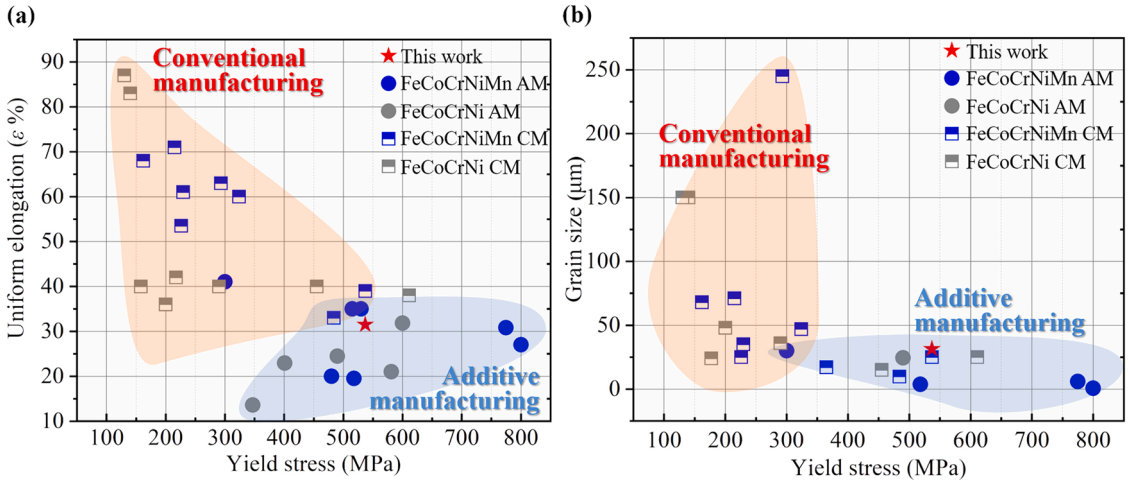

Fig. 6. Comparison of monotonic tensile properties of the present CoCrFeNi L-PBF-HEA with the other CoCrFeNi and CoCrFeMnNi HEAs processed by using conventional and AM routes: (a) a plot of grain size vs. yield strength; and (b) a plot of tensile ductility vs. yield strength. CM: conventional manufacturing; AM: additive manufacturing.

Table 1
Comparison of monotonic tensile properties of CoCrFeNi and CoCrFeMnNi HEAs processed by using conventional and AM routes. The following abbreviations are used for processing method: MLM (magnetic levitation melting), VIM (vacuum induction melting), ArcM (arc melting), and L-PBF (laser powder bed fusion).

Material	Manufacturing method	Yield stress (MPa)	Elongation (%)	Grain size (μm)	Reference
FeCoCrNiMn	L-PBF	520 ± 10	25 ± 2	30 ± 5	[7]
	MLM	300 800	41 27	0.65 30	[11]
	L-PBF	774.8	30.8	5.98	[12]
	VIM	291.3	63.1	–	
	VIM	293.1	63	245.48	[10]
	ArcM	324	60	47	[38]
FeCoCrNi	L-PBF	347 ± 19 401 ± 13 350 ± 12 600 ± 5 489 ± 9	13.6 ± 0.51 22.95 ± 1.47 21.25 ± 1.27 31.85 ± 1.15 24.45 ± 0.75	– 25	[39]
	L-PBF	581.9	22	–	[40]
	ArcM	177	24	–	[41]
	ArcM	130 140	87 83	150 150	[42]
	VIM	611	38	25	[43]
	VIM	455	40	15	[44]

within a grain, although intersection of two sets of twins can occur (the grain in the center of Fig. 10d). With regard to the high-cycle fatigue under the $R = -1$, the CoCrFeMnNi HEA studied by Ghomsheh et al. [9], CoCrFeMnNi HEA studied by Tian et al. [11], and $Al_{0.3}$CoCrFeNi HEA studied by Liu et al. [50] all revealed one set of parallel twins within a grain. This can be attributed to the dislocation annihilation under reversed movement. Only at very localized region of high dislocation accumulation, twins with a certain slip system can be developed. Thus, the presence of the interlaced twin groups under the $R = 0.1$ fatigue condition as shown in Fig. 10d is of interest. Two possible reasons are given below: first, they are induced by the continuous pile-up of dislocations to the grain boundary; second, the pre-existing dislocation cellular structures in the as-built condition facilitate the twin formation with more than one set of twin systems.

The EBSD derived CSL distribution maps clearly delineate the morphology of twins, with 67.9% and 64.8% of them being the $\sum 3$ types, Figs. 10b and 10e, respectively. In addition, the Schmid factor maps in Figs. 10c and 10f indicate that the grains with high twinning activity are the ones orientated for easy dislocation slip, i.e. high Schmid factor. The twin nucleation in fcc material with relatively low SFE (i.e., CoCrFeNi-based HEAs) at low temperatures has been proven by many researchers [37,51,52]. Especially, Otto et al. [52] commented that the deformation twin was rarely observed in CoCrFeMnNi HEA after room temperature tensile deformation by studying various grain sizes. However, the work by Laplanche et al. [37] concluded that a large tensile strain of > 20% can trigger the twin formation at room temperature, and the level of critical stress depends on the material type, grain size and orientation.

For the present CoCrFeNi L-PBF-HEA, a correlation seemed to exist between the crystallographic orientation and twin formation, at first glance of Fig. 9a, Figs. 10a and 10d, with a higher tendency for the $< 110 >$ and $< 001 >$ orientations. Out of the total 354 grains in Fig. 9a, 102 grains fell into the $< 110 >$ orientation group, while 78 grains belonged to the $< 001 >$ group. The remaining 297 grains represented the group having the other orientations. 36 out of 102 grains having the $< 110 >$ orientation exhibited twinning feature, resulting in a high twinned area fraction of 81%. By contrast, 26 out of 78 grains for the $< 001 >$ orientation exhibited a twinning feature, resulting in a high twinned area fraction of 63%. Moreover, only 17 grains out of the remaining 297 grains, with the other orientations (neither $<110 >$ nor $<001 >$), exhibited twinning, with a very low twinned area fraction of 6%. Koyama et al. [53] studied the formation mechanism of twinning inside grains with different orientations, and they concluded that twinning was more likely observed in $< 144 >$, $< 110 >$, and $< 111 >$ grains.

However, drawing a conclusion about the effect of orientation on twin formation in the present CoCrFeNi L-PBF-HEA during high-cycle fatigue must be treated with extra caution. This is because grains with the other orientations (4.74 μm in equivalent diameter) were much smaller than those with $< 001 >$ and $< 110 >$ orientations, with the respective size of 11.29 μm and 12.47 μm. Rahman et al. [54] calculated twin initiation stress for different grain sizes, and it was concluded that the twin nucleation stress increased with the decreasing grain size. To further substantiate the above-mentioned EBSD observation, further data analysis was performed on the specimen subjected to the high-stress fatigue, by selecting several heavily twinned grains with grain size of close to 40 μm but having different grain orientations. It

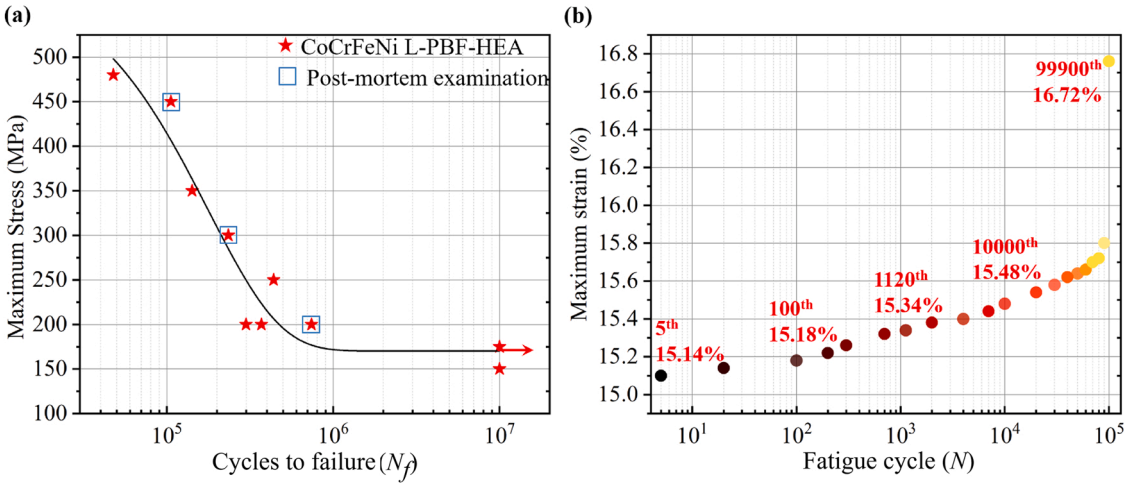

Fig. 7. High-cycle fatigue of CoCrFeNi L-PBF-HEA: (a) *S-N* curve with the specimens used for the post-mortem examination indicated by the square box; (b) a plot of the measured maximum strain vs. fatigue cycles for the specimen tested under the maximum stress of $\sigma_{max} = 450$ MPa with a fatigue life of $N_f = 1.06 \times 10^5$. Note: all fatigue tests in the present work were performed at room temperature and under a stress ratio of $R = 0.1$.

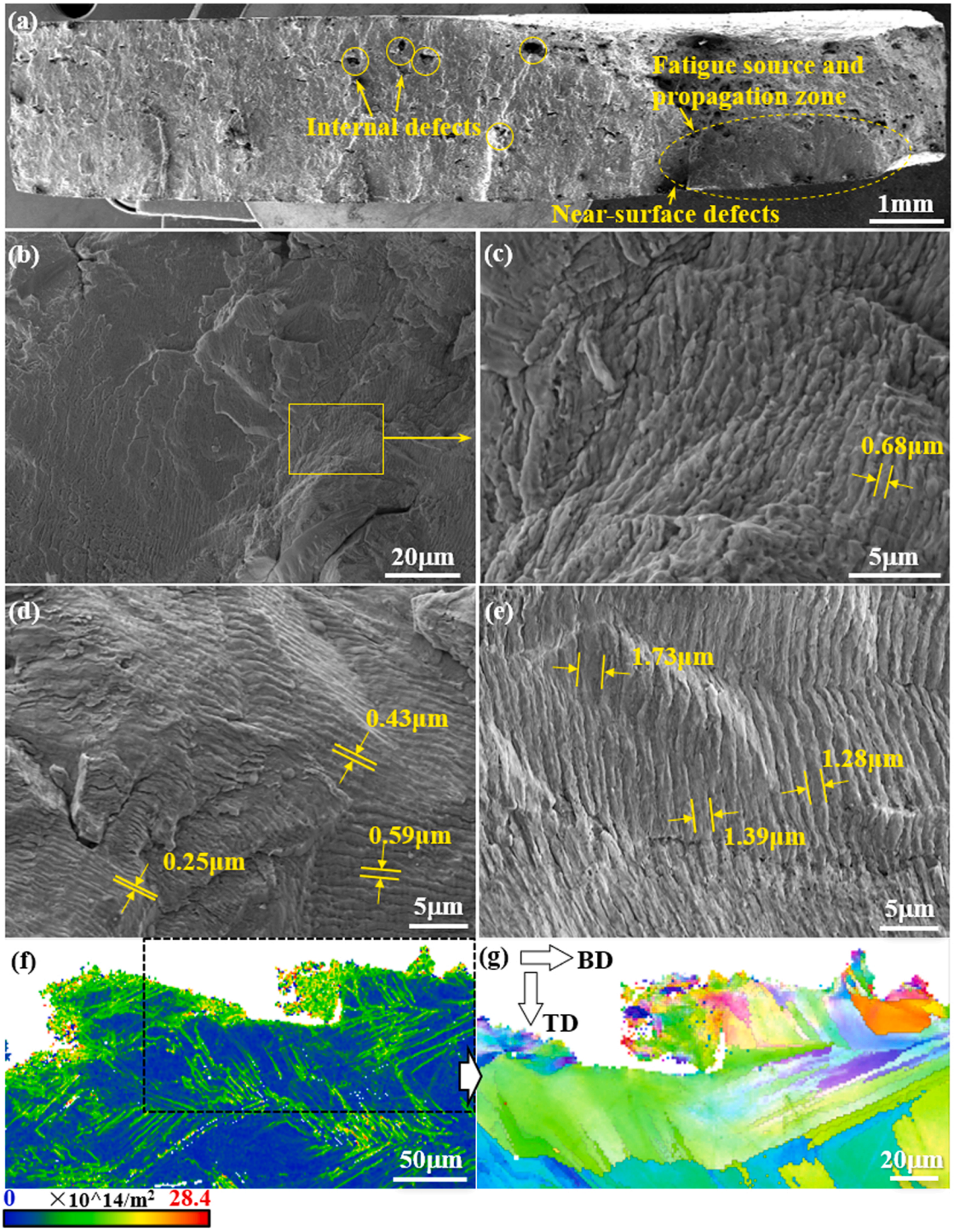

Fig. 8. Post-mortem examination of fatigue failed specimens: (a) to (c) specimen tested at σ_{max}= 300 MPa with N_f= 2.80 × 10^5; (d) specimen tested at σ_{max}= 200 MPa with N_f= 7.40 × 10^5; (e) specimen tested at σ_{max}= 450 MPa with N_f= 1.06 × 10^5; (f) GND map and (g) EBSD IPF-BD orientation map for the specimen tested at σ_{max}= 300 MPa.

was found that in the grains of 41.58 μm, 41.27 μm, and 43.62 μm, near the < 114 > orientation, the twinned area accounted for 6.18%, 0.40% and 5.40% of the grain area, respectively. By contrast, in the grains of 36.64 μm, 35.50 μm, and 43.93 μm, near the < 110 > orientation, the twinned area accounted for 9.23%, 5.69% and 7.19% of the grain area, respectively. This indicates that with the similar grain size, twin formation tendency is higher for the grains near the < 110 > orientation. To summarize, both the present finding and the previous work [53–55] indicate that the twinning tendency is affected by the grain size as well as the grain orientation.

The GND distribution map of the high-stress condition is compared with that of the low-stress condition, Fig. 9d vs. 9e. Under the low-stress fatigue, dislocations tended to accumulate at grain boundaries with the maximum GND value of 35.31 × 10^{14}/m^2, resulting in a distinctive contrast between the grain interior and boundaries, Fig. 9e. Recall that in the as-printed condition, the maximum GND value was measured to be 19.02 × 10^{14}/m^2. Thus, dislocation activity seems to be high even in the case of low-stress fatigue. Under high-stress fatigue, the distribution

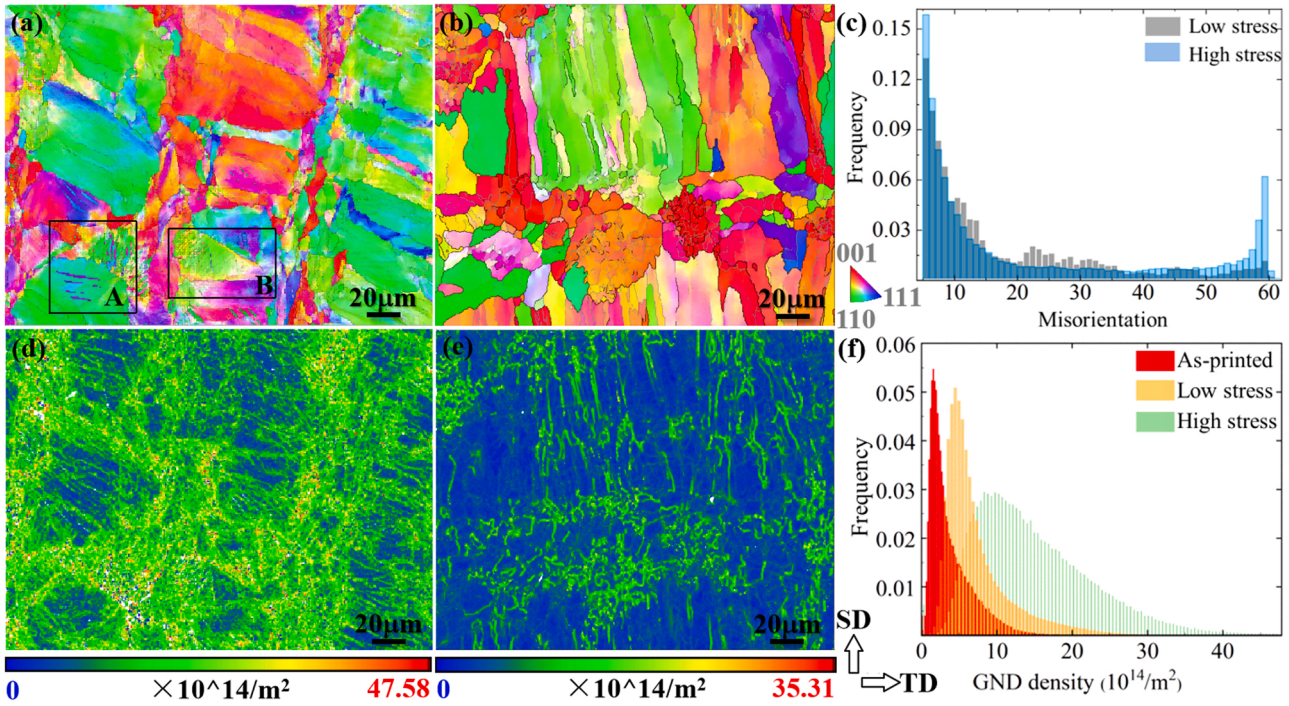

Fig. 9. EBSD analysis on the post-fatigued specimen tested at σ_{max}= 450 MPa with N_f= 1.06 × 10^5 (i.e., high stress condition) in comparison with that tested at σ_{max}= 200 MPa with N_f= 7.40 × 10^5 (i.e., low stress condition): IPF-BD orientation maps of SD-TD cross-section from the high-stress in (a) and low-stress specimens in (b); (c) correlated misorientation distribution histograms; GND distribution maps from the high-stress in (d) and low-stress fatigue conditions in (e); (f) GND distribution histograms.

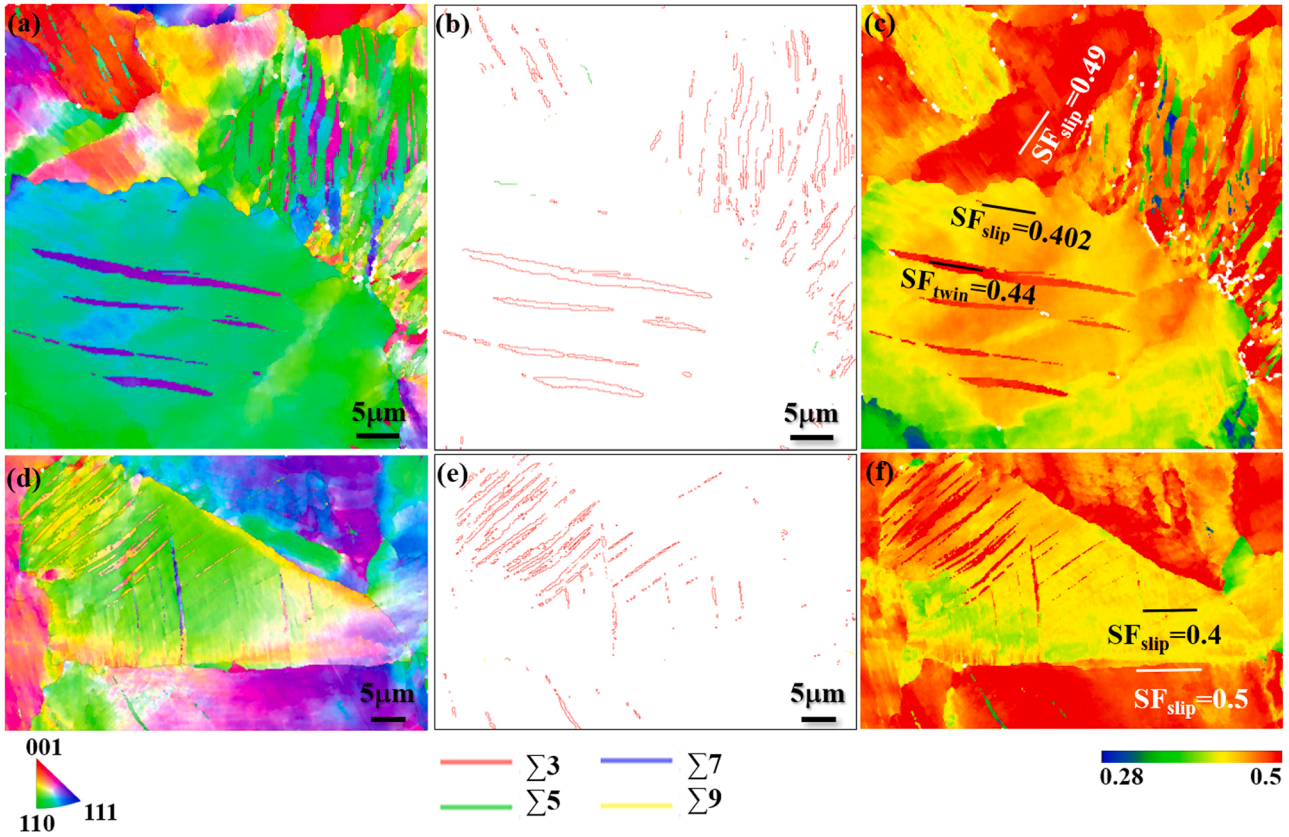

Fig. 10. EBSD results of the enlarged view of region 'A′ and 'B′ as indicated in Fig. 9a: (a) IPF-BD, (b) CSL distribution, and (c) Schmid factor maps for region 'A′; and (d) IPF-BD, (e) CSL distribution, and (f) Schmid factor maps of region 'B′. Note that Schmid factor for the slip is denoted as the "SF_{slip}", while Schmid factor for the twins is denoted as the "SF_{twin}" in the figures.

of dislocations was found to be comparatively homogeneous, with the maximum GND value being 47.58 × 10^{14}/m^2. Fig. 9f compares the GND histograms obtained from the as-built, low-stress and high-stress conditions. Both the low-stress and as-built conditions have a similar profile, but the high-stress has a higher average value but much lower frequency, resulting in a long tail. This indicates that dislocation motion was active in the case of high-stress conditions. Indeed, the comparison of the correlated misorientation distribution histograms (Fig. 9c) leads to a similar conclusion. First, the increased fraction of LAGBs suggests a higher dislocation activity under high-stress fatigue. Second, the presence of 60° misorientation peak in the high-stress condition confirms the twinning activity as observed in Fig. 9a, Figs. 10a and 10d.

To better understand the dislocation activity during the high-cycle fatigue, TEM was used to examine both the high-stress and low-stress fatigue conditions. Fig. 11a shows the bright-field TEM image of the low-stress condition, revealing many dislocation cells. The enlarged view of Fig. 11b clearly shows the presence of dislocation tangles at cell interiors, while the cell walls are composed of dense dislocations. By comparison, the high-stress fatigue sample shows much less dislocations in the cell interior, accompanied by the more well-defined boundaries, Fig. 11c. The size of the dislocation cells decreased with the higher fatigue stress, which is consistent with the previous work [7]. Such a reduced dislocation cell size can satisfactorily explain the material strengthening as observed in our micro-hardness measurements (210 ± 10.1 $HV_{0.2}$ as opposed to 268 ± 7.7 $HV_{0.2}$ for the test condition of σ_{max}=200 MPa and 450 MPa). The distribution of dislocations at the wall of cellular structure is shown in Fig. 11d, where dislocation slip traces are visible close to the wall together with evidence to indicate high dislocation activity within the wall.

The formation of sub-grains (i.e., with the well-defined boundary) is under the high-cycle fatigue stress, and largely due to the pre-existing dislocation cellular structures as observed in Fig. 3 for the as-built condition. Although the materials with low SFE, including the present CoCrFeNi HEA, are difficult to activate dislocation cross-slip, the dislocation cellular structure due to the L-PBF process seems to plays an important role in the sub-grain formation. During cyclic loading, dislocations move back and forth within a certain range, resulting in dislocation annihilation, dissociation and re-arrangement. The dislocation re-arrangement tends to form a lower energy configuration, namely cellular structure or sub-grains with alternating high and low-density dislocation regions [56]. Such a re-arrangement process is known as dynamic recovery and/or recrystallisation, which is driven by a reduction in the overall stored strain energy associated with the elastic dislocation interaction [57]. In this regard, there is little difference in terms of the dislocation re-arrangement under cyclic loading between the CoCrFeNi L-PBF-HEA (Figs. 11a to 11d) and the traditional alloys (e.g. Type 316 austenitic stainless steel [58,59]).

In summary, we observed a high dislocation activity at the wall region of cellular structure in CoCrFeNi L-PBF-HEA during high-cycle fatigue. Figs. 11e to 11g provide the schematics describing how dislocation is re-arranged under high-stress and low-stress fatigue conditions. For the high-stress condition, dislocation walls at the cell boundaries were more well-defined, accompanied by far fewer dislocation tangles and single dislocations at the cell interiors. The schematic of the as-built condition (Fig. 11e) was created according to the TEM observation in Fig. 3. Under low-stress conditions (Fig. 11f), highly dissociated dislocations could not cross slip as their far-apart partials belong to only one {111} plane [60]. Additional stress is required to

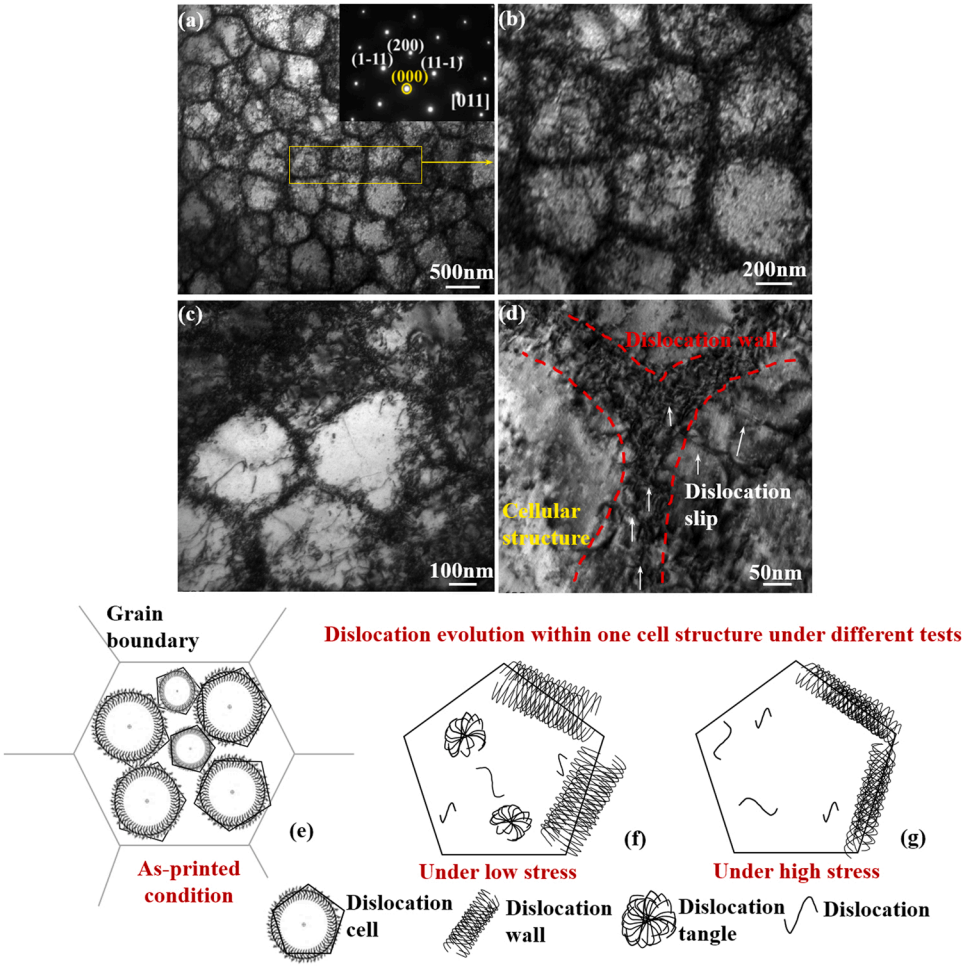

Fig. 11. TEM analysis performed on the SD-TD cross-section of the post-fatigued specimens: (a) and (b) low-stress condition of σ_{max}= 200 MPa; (c) and (d) high-stress condition of σ_{max}= 450 MPa. Inset in (a) is the selected area electron diffraction pattern from which figure (a) was taken from the [011] zone axis. (e) to (g) schematics showing the cellular structure evolution during high-cycle fatigue under low-stress in (f) and high-stress in (g), in comparison with that of the as-built condition in (e).

recombine these dislocations into a cross-slip favorable configuration. When the fatigue stress is increased (i.e., high-stress condition), the leading partial dislocations can overcome the boundary barrier and slip into the neighboring boundary, contributing to the formation of well-defined dislocation walls [25,61].

3.5. Nano-twinning mechanism during high-cycle fatigue

Deformation twinning has been recognized as the predominant deformation mechanism responsible for the lack of a strength-ductility trade-off in CoCrFeNi-based HEA during monotonic tensile loading. Concerning the cyclic loading, contradictory results exist in terms of whether twinning can occur during the high-cycle fatigue at room temperature. The EBSD observation in Fig. 9 and Fig. 10 on the high-stress specimen with a fatigue life $N_f = 1.06 \times 10^5$ provides evidence of deformation twins. But, it is still not clear about the twin formation mechanism for the CoCrFeNi L-PBF-HEA during high-cycle fatigue.

Fig. 12a provides the TEM overview of a representative region taken from the high-stress specimen. This region contains both the deformation twins and the cellular dislocation structure. A highly distorted lattice within the cellular structure, as presented in Fig. 12b, an HRTEM atomic-resolution image, shows high local deformation. Stacking faults (SFs) can be clearly seen in the region highlighted in Fig. 12d. A couple of full dislocations have been indicated in Fig. 12b with an enlarged view given in Fig. 12e. The formation of SFs at the region of cellular structure is attributed to the high density of dislocations. Dislocations at the cell walls are expected to undergo a much wider dissociation than those away from it, increasing the tendency to form SFs. It was commented in [25] that SFs facilitated twin nucleation upon plastic deformation. This probably explains the co-existence of twins and cellular structure in the post-fatigued condition (Fig. 12a). An et al. [62] studied the twin formation mechanism in cyclic loading of fcc Cu. They reported that under the cyclic loading, partial dislocations emitted from the grain boundaries slip back-and-forth on the {111} plane and eventually form the twin nuclei within the grain.

To illustrate the high dislocation activity more clearly, a TEM image taken from the [011] zone axis is shown in Fig. 12c, where heavily tangled dislocations, as well as the so-called labyrinth wall-like dislocation structure [63], can be seen. The cell boundaries containing a high density of tangled dislocations (Fig. 12c) are expected to help hinder dislocation motion. The newly generated dislocations during the high-cycle fatigue would be impeded by the cell walls, which limits the mean free path within the scale of the cells. The interaction between the cell boundaries and free dislocations can be in the form of SFs, partial

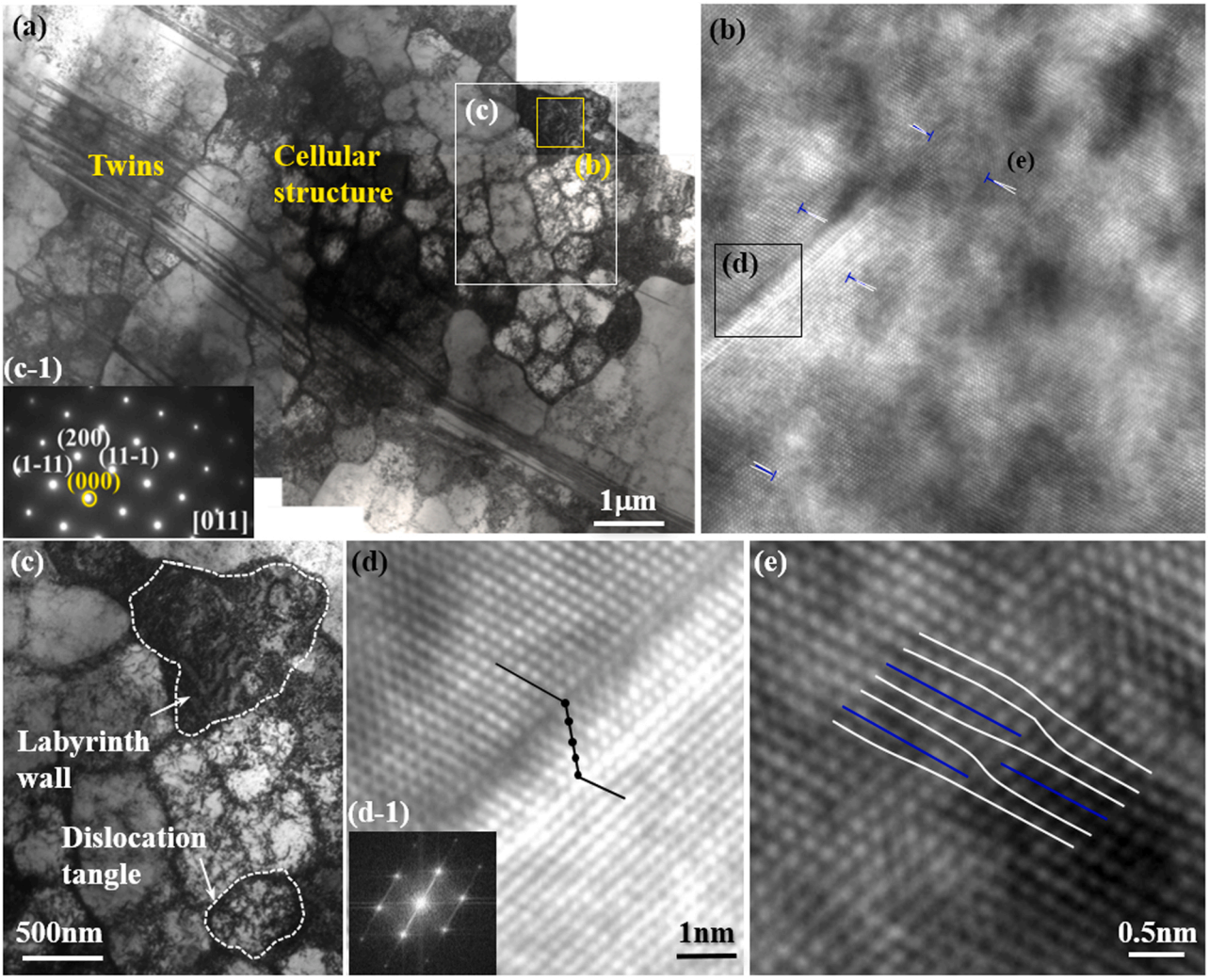

Fig. 12. (a) An overview TEM image showing the co-existence of cellular structure and nano-twins in the specimen after high-stress fatigue; (b) an HRTEM image of the yellow box highlighted region in (a) showing lots of full dislocations and stacking faults within the cellular structure; (c) a closed view of the white box highlighted region in (a) showing the formation of labyrinth wall-like dislocation structure as well as dislocation tangles as viewed under the zone axis of [011] in (c-1); (d) an enlargement of the black rectangle highlighted region in (b) showing the stacking faults (SFs) as confirmed by the FFT image in (d-1); (e) the region 'e' enlargement in (b) identifying full dislocations.

dislocations and full dislocations, which would appear in the vicinity of cell boundaries. This potentially can provide a 3D impediment network for the dislocation motion, particularly in the later stage of the fatigue test, acting as the barrier to crack propagation [64]. On the other hand, these defects can facilitate dislocation nucleation by generating stress concentrations at the interface [58].

Fig. 13a presents a bundle of parallel nano-twins as revealed by TEM bright-field imaging. The corresponding dark-field image, as shown in Fig. 13b, permitted us to measure the twin thickness, being in the order of tens of nanometers with the size ranging from 2.37 nm to 24.83 nm. The selected area diffraction (SAD) pattern taken from the region as indicated in Fig. 13a and indexed in Fig. 13c clearly illustrate the orientation relationship between the twin and matrix. A series of HRTEM images taken from the twinned region are shown in Fig. 13d to 1f, together with their enlarged views in Fig. 13d-1 to f-1. Various types of lattice defects are identified in the twinned region, including full dislocations, partial dislocations, distortions, and SFs. The inverse fast Fourier transform (FFT) images were used to help identify the full and partial dislocations ambiguously, with exemplars shown in Fig. 13g, h, and i. According to the literature [23,27,52,65–69], it is likely that the identified partial dislocations are $1/6 < 112 >$ Shockley partials, which is crucial for the twin formation. This is because that the early-stage plastic deformation occurs by the glide of $1/2 < 110 >$ dislocations dissociated into $1/6 < 112 >$ Shockley partials on {111} planes, as observed in CoCrFeNi in [69], CoCrFeMnNi in [52] and Fe-Mn-C steel [65].

The twin formation mechanisms of fcc metals, including the CoCrFeNi HEA, are summarized as follows [23]:

1) The partial dislocation mechanism proposed by Venables and Hirth [70]:
   $a/2 < 110 > \rightarrow a/6 < 41\text{–}1 > + a/6 < 12\text{–}1 >$
2) Cross-slip of stair-rod dislocation mechanism proposed by Weertman and Fujita [71]:
   $a/2 < 101 > \rightarrow a/6 < 121 > + a/3 < 1\text{–}11 >$
3) The extrinsic stacking fault mechanism proposed by Mahajan and Chin [65]:
   $a/2 < 011 > + a/2 < -101 > \rightarrow 3 \times a/6 < 12\text{–}1 >$.

They all involve reactions from $a/2 < 110 >$ to $a/6 < 112 >$, despite their difference in the dislocation types. Laplanche [69] summarized the TEM observation of dislocations in CoCrNi medium entropy alloy and CoCrFeNiMn HEA. In the early stage of plasticity, $1/2 < 110 >$ was observed to decompose into Shockley partial dislocation $1/6 < 112 >$ on {111} plane, and the Shockley dislocation glided continuously on the {111} plane to form twins. In the present work, we observed partial dislocations near the twins and in the areas where twins did not appear. It is thus claimed that the twinning mechanism in CoCrFeNi L-PBF-HEA was likely to be consistent with that of the conventional fcc metals, namely, the full dislocation $a/2 < 110 >$ decomposed to the Shockley partial dislocation $a/6 < 112 >$. Note that the partial dislocation can either be an Frank partial dislocation $1/3 < 111 >$ or Shockley partial dislocation $1/6 < 112 >$; its discrimination is beyond the scope of the present work.

In this work, the nano-twinning induced by high-stress fatigue at $R = 0.1$ seems to be different from that induced by monotonic tensile loading, as sketched in Fig. 14. For the monotonic loading scenario, primary twins are formed in the early stage (Fig. 14b_1), followed by the development of secondary twins. The development of secondary twins is characterized by a ~70° angle relative to the primary twins (Fig. 14 b_2). Further loading would trigger the formation of tertiary twins (Fig. 14 b_3), but again they have a certain angle (usually about 70°) with the secondary twin boundaries. After the formation of primary twins, Shockley dislocations continue to glide on the (−111) plane between the primary twins, forming a kink structure of five to seven atomic layers, with the atoms inclined clockwise by about 18.5° at the kink interface. As a result, the angle between the secondary twin and the primary twin becomes 71.5° [72]. In the work by Chen et al. [73], the angle between the primary and secondary twins was also found to be ~70°, despite a different angle between the primary twin and tensile loading direction.

Furthermore, twin thickness induced under monotonic tensile loading are relatively stable [68]. However, refer to the EBSD observations in Fig. 9 and Fig. 10, two types of twins are observed after high-stress fatigue loading: micro-twins and nano-twins. This may suggest that twinning formed during high-cycle fatigue is less stable. Also, it is interesting to note that the nano-twins are not always parallel to each other (a combination of the schematics in Fig. 14 c_2 and $c_{2'}$). Such inclined nano-twins might be due to the absence of compressive stress, which deserves further study.

The presence of deformation twins on high-cycle fatigue properties is twofold: first, twinning can promote the dynamic Hall-Petch effect [52,69,74] by introducing extra boundaries that act as barriers to dislocation motion; second, twin boundaries also allow dislocations to slip and penetrate. The latter helps to release stress concentration to a certain extent, and this mechanism was found to retain a good level of ductility whilst enhancing the material strength [75]. Especially, Sidharth et al. [3] compared fatigue crack growth behavior of the $< 001 >$ and $< 111 >$ single-crystal CoCrFeMnNi HEA and they found that twining activated by plastic deformation in $< 001 >$ grains delayed the inception of the unstable stage III regime in fatigue crack growth. Moreover, Liu and Zhou [76] reported that twin boundaries provide more local sites for accommodating dislocations, promoting the emission of dislocations from the crack tip, leading to strong crack blunting and high fracture toughness. In terms of strength enhancement, dislocations near twin boundaries may dissociate with residing and moving along the twin boundary or with one partial passing through the boundary and gliding in a conjugate slip system. Therefore, the existing twins serve as effective barriers for the latter twins, contributing to strain hardening during plastic deformation [6,65,77–79]. Our micro-hardness measurement result on the post-fatigued specimen seems to support the above-mentioned strengthening mechanism as we observed a hardness elevation of ~80 $HV_{0.2}$ by comparison of the σ_{max}= 450 MPa fatigued sample with the as-built condition.

4. Conclusions

The main conclusions are summarized as follows:

1) The as-built CoCrFeNi L-PBF-HEA is characterized by the combination of $< 001 >$ and $< 110 >$ texture, a high proportion of low-angle boundaries suggesting the presence of cellular dislocation substructure as well as reasonably high tensile strength.
2) After high-cycle fatigue at σ_{max}= 450 MPa (R=0.1) with a life of $N_f = 1.06 \times 10^5$, deformation twins were triggered primarily in the grains with $< 001 >$ and $< 110 >$ orientations. These fatigue-induced twins contribute to the bulk cyclic softening behavior as manifested from the data curve of maximum strain vs. fatigue cycles. At the microscopic level, deformation twins clearly lead to the hardness elevation from 189 ± 6.7 $HV_{0.2}$ in the as-built condition to 268 ± 7.7 $HV_{0.2}$ in the post-fatigued condition within the region with the twinning feature.
3) By comparison, after high-cycle fatigue at the lower stress level of σ_{max}= 300 MPa and 200 MPa (R=0.1) with a life of $N_f = 2.80 \times 10^5$ and 7.40×10^5, respectively, there was no evidence for the occurrence of twinning. This concurs with the micro-hardness value for the low-stress fatigue condition, namely 210 ± 10.1 $HV_{0.2}$ as measured on the specimen tested at σ_{max}= 200 MPa.
4) The underlying mechanism for the formation of nano-twins during high-stress fatigue of σ_{max}= 450 MPa was likely attributed to the dissociation of $1/2 < 110 >$ full dislocations to $1/6 < 112 >$ partial

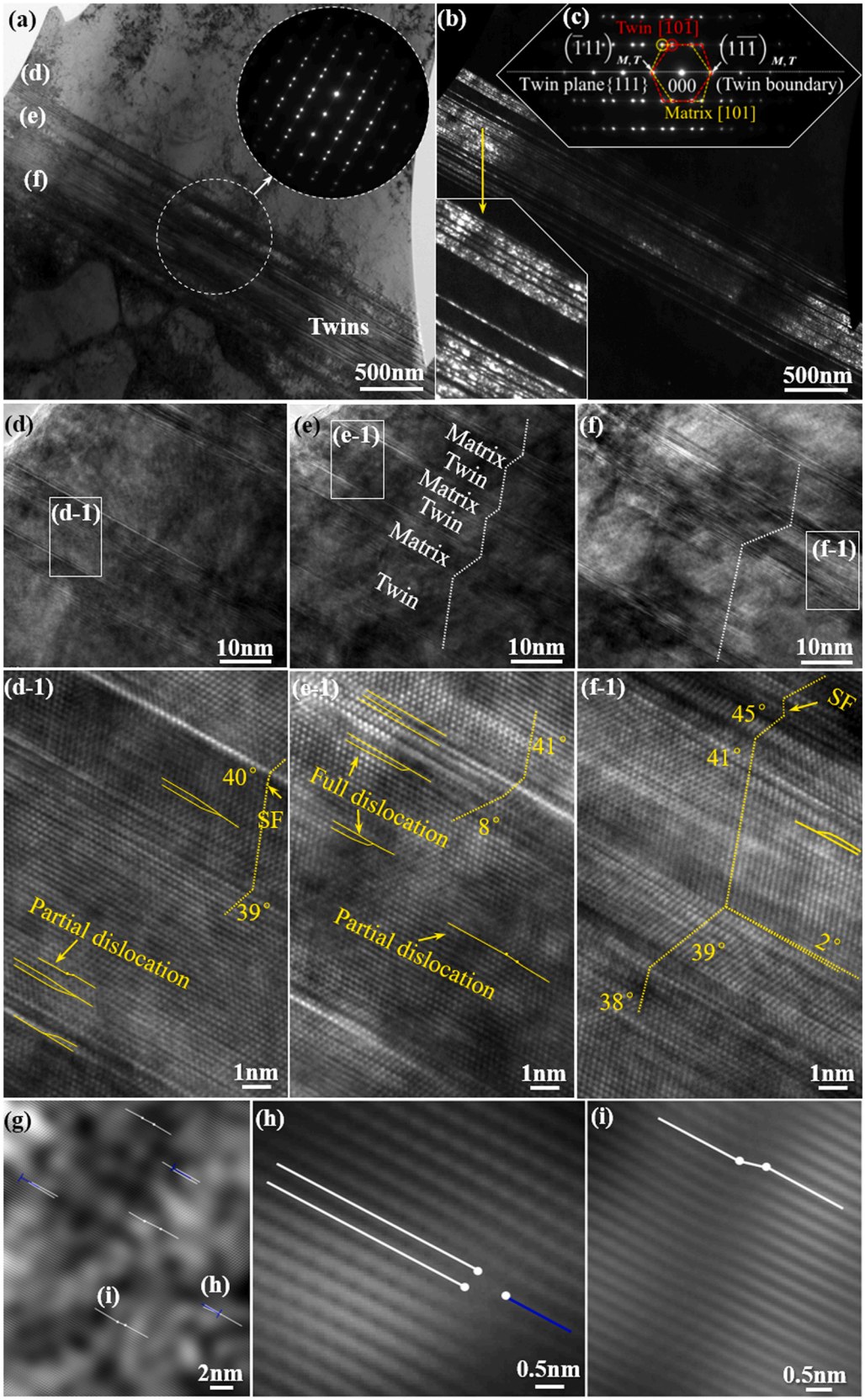

Fig. 13. (a) an overview TEM image showing the twin structure of the high-stress fatigue condition together with the SAD pattern confirmation; (b) the corresponding dark-field image of the same region, showing the twin boundary and twin thickness; (c) detailed information of the inset SAD pattern in (a) and (b) with [101] zone axis showing the orientation relationship of the twin and matrix. (d) to (f) HRTEM images of the corresponding region in (a); (d-1) to (f-1) close views of the white rectangle regions ''d-1'', ''e-1'', ''f-1'' in (d) to (f), showing full dislocations, partial dislocations, distortions, and stacking faults near the junction and the angle between twin and matrix. (g) to (i) inverse FFT images taken from a twinned region with close views given in (h) and (i). (h) close view of region ''h'' showing full dislocation; (i) close view of the region ''i'' showing partial dislocation.

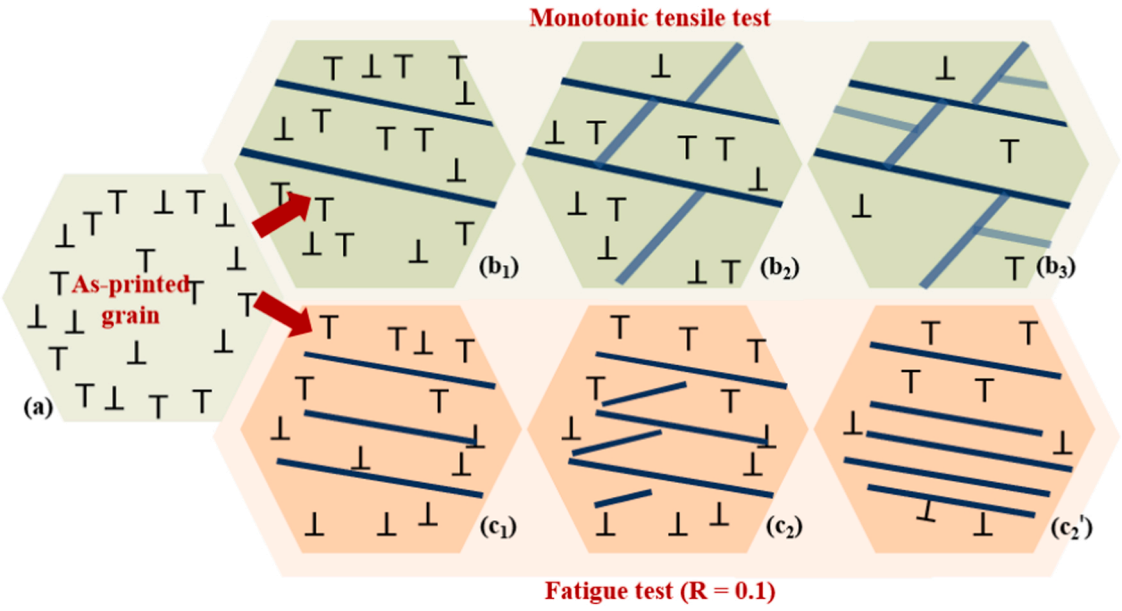

Fig. 14. Schematics describing the twin formation mechanisms: (a) as-built condition; (b) after monotonic tensile deformation; (c) after cyclic fatigue. Under monotonic loading, primary twins form (b_1), followed by the secondary twins (b_2), which have a 70° angle with respect to the primary twins, and tertiary twins (b_3), which also have 70° angle with respect to the secondary twins. Under fatigue loading, nano-twins nucleate within a grain, followed by the formation of other nano-twins inclined (c_2) or parallel to (c_2') the primary ones.

ones, given the TEM and HRTEM observation of full and partial dislocations, lattice distortion and stacking faults.

5) Besides, the cellular structures formed in the as-built condition tends to develop further to a well-defined sub-grain structure as a result of high-stress fatigue loading.

Associated Content

The Supporting Information is available at the Supplementary Material File. X-ray diffraction measurement on the as-built sample (Fig. S1); SEM-based EDS mapping on the as-built sample after the fatigue failure (Fig. S2); Schematic of grain growth direction in relation to the laser-beam scanning (Fig. S3); EBSD determined misorientation distribution maps on the as-built sample (Fig. S4); EBSD-detected twin identification based on the CSL map (Fig. S5).

CRediT authorship contribution statement

Yinan Chen: Writing – original draft, Methodology, Investigation, Data curation. **Bo Li:** Writing – original draft, Visualization, Validation, Resources, Investigation, Funding acquisition. **Bo Chen:** Writing – review & editing, Visualization, Validation, Methodology, Funding acquisition, Conceptualization. **Fuzhen Xuan:** Supervision, Resources, Methodology, Conceptualization.

Declaration of Competing Interest

The authors declare that they have no known competing financial interests or personal relationships that could have appeared to influence the work reported in this paper.

Data Availability

Data will be made available on request.

Acknowledgement

This work is financially sponsored by National Natural Science Foundation of China (Grant No. 52175140), Natural Science Foundation of Shanghai, in China (Grant No. 20ZR1414000), International Collaboration Program from Science and Technology Commission of Shanghai Municipality, China (Grant No. 19110712500). Bo Chen acknowledges financial supports by the UK's Engineering and Physical Sciences Research Council, EPSRC Early Career Fellowship Scheme EP/R043973/1 and East China University of Science and Technology (ECUST) through the Ministry of Education of the People's Republic of China 'the 111 Project'. Bo Chen is very grateful for Prof Shan-Tung Tu at ECUST who has been consistently introducing many opportunities and providing resources to allow Bo Chen to develop new collaborations.

Appendix A. Supporting information

Supplementary data associated with this article can be found in the online version at doi:10.1016/j.addma.2022.103319.

References

[1] E.P. George, W.A. Curtin, C.C. Tasan, High entropy alloys: a focused review of mechanical properties and deformation mechanisms, Acta Mater. 188 (2020) 435–474, https://doi.org/10.1016/j.actamat.2019.12.015.

[2] T.N. Lam, S.Y. Lee, N.T. Tsou, H.S. Chou, B.H. Lai, Y.J. Chang, R. Feng, T. Kawasaki, S. Harjo, P.K. Liaw, A.C. Yeh, M.J. Li, R.F. Cai, S.C. Lo, E.W. Huang, Enhancement of fatigue resistance by overload-induced deformation twinning in a CoCrFeMnNi high-entropy alloy, Acta Mater. 201 (2020) 412–424, https://doi.org/10.1016/j.actamat.2020.10.016.

[3] R. Sidharth, W. Abuzaid, H. Sehitoglu, Nano-twinning enhanced room temperature fatigue crack growth in single crystalline CoCrFeMnNi high entropy alloy, Intermetallics 126 (2020), 106919, https://doi.org/10.1016/j.intermet.2020.106919.

[4] W. Li, X. Long, S. Huang, Q. Fang, C. Jiang, Elevated fatigue crack growth resistance of Mo alloyed CoCrFeNi high entropy alloys, Eng. Fract. Mech. 218 (106579) (2019) 1–9, https://doi.org/10.1016/j.engfracmech.2019.106579.

[5] W.M. Williams, M. Shabani, P.D. Jablonski, G.J. Pataky, Fatigue crack growth behavior of the quaternary 3d transition metal high entropy alloy CoCrFeNi, Int. J. Fatigue 148 (106232) (2021) 1–9, https://doi.org/10.1016/j.ijfatigue.2021.106232.

[6] K.V.S. Thurston, B. Gludovatz, A. Hohenwarter, G. Laplanche, E.P. George, R. O. Ritchie, Effect of temperature on the fatigue-crack growth behavior of the high-entropy alloy CrMnFeCoNi, Intermetallics 88 (2017) 65–72, https://doi.org/10.1016/j.intermet.2017.05.009.

[7] M. Jin, A. Piglione, B. Dovgyy, E. Hosseini, P.A. Hooper, S.R. Holdsworth, M. Pham, Cyclic plasticity and fatigue damage of CrMnFeCoNi high entropy alloy fabricated by laser powder-bed fusion, Addit. Manuf. 36 (101584) (2020) 1–5, https://doi.org/10.1016/j.addma.2020.101584.
[8] K. Lu, A. Chauhan, D. Litvinov, M. Walter, A.S. Tirunilai, J. Freudenberger, A. Kauffmann, M. Heilmaier, J. Aktaa, High-temperature low cycle fatigue behavior of an equiatomic CoCrFeMnNi high-entropy alloy, Mater. Sci. Eng. A 791 (139781) (2020) 1–12, https://doi.org/10.1016/j.msea.2020.139781.
[9] M.Z. Ghomsheh, G. Khatibi, B. Weiss, M. Lederer, S. Schwarz, A. Steiger-Thirsfeld, M.A. Tikhonovsky, E.D. Tabachnikova, E. Schafler, High cycle fatigue deformation mechanisms of a single phase CrMnFeCoNi high entropy alloy, Mater. Sci. Eng. A 777 (2020), https://doi.org/10.1016/j.msea.2020.139034.
[10] Y. Kim, G. Ham, H.S. Kim, K. Lee, High-cycle fatigue and tensile deformation behaviors of coarse-grained equiatomic CoCrFeMnNi high entropy alloy and unexpected hardening behavior during cyclic loading, Intermetallics 111 (106486) (2019) 1–9, https://doi.org/10.1016/j.intermet.2019.106486.
[11] Y.Z. Tian, S.J. Sun, H.R. Lin, Z.F. Zhang, Fatigue behavior of CoCrFeMnNi high-entropy alloy under fully reversed cyclic deformation, J. Mater. Sci. Technol. 35 (2019) 334–340, https://doi.org/10.1016/j.jmst.2018.09.068.
[12] Y.K. Kim, M.S. Baek, S. Yang, K.A. Lee, In-situ formed oxide enables extraordinary high-cycle fatigue resistance in additively manufactured CoCrFeMnNi high-entropy alloy, Addit. Manuf. 38 (2021), 101832, https://doi.org/10.1016/j.addma.2020.101832.
[13] A.G. Wang, X.H. An, J. Gu, X.G. Wang, L.L. Li, W.L. Li, M. Song, Q.Q. Duan, Z. F. Zhang, X.Z. Liao, Effect of grain size on fatigue cracking at twin boundaries in a CoCrFeMnNi high-entropy alloy, J. Mater. Sci. Technol. 39 (2020) 1–6, https://doi.org/10.1016/j.jmst.2019.09.010.
[14] J.M. Park, J. Choe, J.G. Kim, J.W. Bae, J. Moon, S. Yang, K.T. Kim, J.-H. Yu, H. S. Kim, Superior tensile properties of 1%C-CoCrFeMnNi high-entropy alloy additively manufactured by selective laser melting, Mater. Res. Lett. 8 (2020) 1–7, https://doi.org/10.1080/21663831.2019.1638844.
[15] J. Jin, R. Gao, H. Peng, H. Guo, S. Gong, B. Chen, Rapid solidification microstructure and carbide precipitation behavior in electron beam melted high-speed steel, Metall. Mater. Trans. A 51 (2020) 2411–2429, https://doi.org/10.1007/s11661-020-05661-z.
[16] B. Li, B. Qian, Y. Xu, Z. Liu, J. Zhang, F. Xuan, Additive manufacturing of ultrafine-grained austenitic stainless steel matrix composite via vanadium carbide reinforcement addition and selective laser melting: formation mechanism and strengthening effect, Mater. Sci. Eng. A 745 (2019) 495–508, https://doi.org/10.1016/j.msea.2019.01.008.
[17] S. Xiang, J. Li, H. Luan, A. Amar, S. Lu, K. Li, L. Zhang, X. Liu, G. Le, X. Wang, F. Qu, W. Zhang, D. Wang, Q. Li, Effects of process parameters on microstructures and tensile properties of laser melting deposited CrMnFeCoNi high entropy alloys, Mater. Sci. Eng. A 743 (2019) 412–417, https://doi.org/10.1016/j.msea.2018.11.110.
[18] P. Chen, S. Li, Y. Zhou, M. Yan, M.M. Attallah, Fabricating CoCrFeMnNi high entropy alloy via selective laser melting in-situ alloying, J. Mater. Sci. Technol. 43 (2020) 40–43, https://doi.org/10.1016/j.jmst.2020.01.002.
[19] R. Li, P. Niu, T. Yuan, P. Cao, C. Chen, K. Zhou, Selective laser melting of an equiatomic CoCrFeMnNi high-entropy alloy: processability, non-equilibrium microstructure and mechanical property, J. Alloy. Compd. 746 (2018) 125–134, https://doi.org/10.1016/j.jallcom.2018.02.298.
[20] B. Li, L. Zhang, Y. Xu, Z. Liu, B. Qian, F. Xuan, Selective laser melting of CoCrFeNiMn high entropy alloy powder modified with nano-TiN particles for additive manufacturing and strength enhancement: process, particle behavior and effects, Powder Tech. 360 (2020) 509–521, https://doi.org/10.1016/j.powtec.2019.10.068.
[21] B. Li, L. Zhang, B. Yang, Grain refinement and localized amorphization of additively manufactured high-entropy alloy matrix composites reinforced by nano ceramic particles via selective-laser-melting/remelting, Compos. Commun. 19 (2020) 56–60, https://doi.org/10.1016/j.coco.2020.03.001.
[22] Z.G. Zhu, Q.B. Nguyen, F.L. Ng, X.H. An, X.Z. Liao, P.K. Liaw, S.M.L. Nai, J. Wei, Hierarchical microstructure and strengthening mechanisms of a CoCrFeNiMn high entropy alloy additively manufactured by selective laser melting, Scr. Mater. 154 (2018) 20–24, https://doi.org/10.1016/j.scriptamat.2018.05.015.
[23] K.M. Rahman, N.G. Jones, D. Dye, Micromechanics of twinning in a TWIP steel, Mater. Sci. Eng. A 635 (2015) 133–142, https://doi.org/10.1016/j.msea.2015.03.082.
[24] H. Wang, Z.G. Zhu, H. Chen, A.G. Wang, J.Q. Liu, H.W. Liu, R.K. Zheng, S.M.L. Nai, S. Primig, S.S. Babu, S.P. Ringer, X.Z. Liao, Effect of cyclic rapid thermal loadings on the microstructural evolution of a CrMnFeCoNi high-entropy alloy manufactured by selective laser melting, Acta Mater. 196 (2020) 609–625, https://doi.org/10.1016/j.actamat.2020.07.006.
[25] T. Voisin, J.B. Forien, A. Perron, S. Aubry, N. Bertin, A. Samanta, A. Baker, Y. M. Wang, New insights on cellular structures strengthening mechanisms and thermal stability of an austenitic stainless steel fabricated by laser powder-bed-fusion, Acta Mater. 203 (2021), https://doi.org/10.1016/j.actamat.2020.11.018.
[26] T.M. Smith, M.S. Hooshmand, B.D. Esser, F. Otto, D.W. Mccomb, E.P. George, M. Ghazisaeidi, M.J. Mills, Atomic-scale characterization and modeling of 60° dislocations in a high-entropy alloy, Acta Mater. 110 (2016) 352–363, https://doi.org/10.1016/j.actamat.2016.03.045.
[27] A.V. Korchuganov, A.N. Tyumentsev, K.P. Zolnikov, I.Y. Litovchenko, D. S. Kryzhevich, E. Gutmanas, S. Li, Z. Wang, S.G. Psakhie, Nucleation of dislocations and twins in fcc nanocrystals: dynamics of structural transformations, J. Mater. Sci. Technol. 35 (2019) 201–206, https://doi.org/10.1016/j.jmst.2018.09.025.
[28] P. Zhao, B. Chen, Z. Zheng, B. Guan, X. Zhang, S. Tu, Microstructure and texture evolution in a post-dynamic recrystallised titanium during annealing, monotonic and cyclic loading, Metall. Mater. Trans. A. 52 (2021) 394–412, https://doi.org/10.1007/s11661-020-06071-x.
[29] Y. Li, D. Parfitt, P.E.J. Flewitt, X. Hou, J. Quinta de Fonseca, B. Chen, Microstructural considerations of enhanced tensile strength and mechanical constraint in a copper/stainless steel brazed joint, Mater. Sci. Eng. A 796 (139992) (2020) 1–13, https://doi.org/10.1016/j.msea.2020.139992.
[30] D. Wang, C. Song, Y. Yang, Y. Bai, Investigation of crystal growth mechanism during selective laser melting and mechanical property characterization of 316L stainless steel parts, Mater. Des. 100 (2016) 291–299, https://doi.org/10.1016/j.matdes.2016.03.111.
[31] Z.G. Zhu, X.H. An, W.J. Lu, Z.M. Li, F.L. Ng, X.Z. Liao, U. Ramamurty, S.M.L. Nai, J. Wei, Selective laser melting enabling the hierarchically heterogeneous microstructure and excellent mechanical properties in an interstitial solute strengthened high entropy alloy, Mater. Res. Lett. 7 (2019) 453–459, https://doi.org/10.1080/21663831.2019.1650131.
[32] W. Wei, J.C. Xiao, C.F. Wang, Q. Cheng, F.J. Guo, Q. He, M.S. Wang, S.Z. Jiang, C. X. Huang, Hierarchical microstructure and enhanced mechanical properties of SLM-fabricated GH5188 Co-superalloy, Mater. Sci. Eng. A 831 (2022), https://doi.org/10.1016/j.msea.2021.142276.
[33] X. Zhou, K. Li, D. Zhang, X. Liu, J. Ma, W. Liu, Z. Shen, Textures formed in a CoCrMo alloy by selective laser melting, J. Alloy. Compd. 631 (2015) 153–164, https://doi.org/10.1016/j.jallcom.2015.01.096.-.
[34] Y.K. Kim, J. Choe, K.A. Lee, Selective laser melted equiatomic CoCrFeMnNi high-entropy alloy: Microstructure, anisotropic mechanical response, and multiple strengthening mechanism, J. Alloy. Compd. 805 (2019) 680–691, https://doi.org/10.1016/j.jallcom.2019.07.106.
[35] A. Piglione, B. Dovgyy, C. Liu, C.M. Gourlay, P.A. Hooper, M.S. Pham, Printability and microstructure of the CoCrFeMnNi high-entropy alloy fabricated by laser powder bed fusion, Mater. Lett. 224 (2018) 22–25, https://doi.org/10.1016/j.matlet.2018.04.052.
[36] C. Lee, G. Song, M.C. Gao, R. Feng, P. Chen, J. Brechtl, Y. Chen, K. An, W. Guo, J. D. Poplawsky, S. Li, A.T. Samaei, W. Chen, A. Hu, H. Choo, P.K. Liaw, Lattice distortion in a strong and ductile refractory high-entropy alloy, Acta Mater. 160 (2018) 158–172, https://doi.org/10.1016/j.actamat.2018.08.053.
[37] G. Laplanche, A. Kostka, O.M. Horst, G. Eggeler, E.P. George, Microstructure evolution and critical stress for twinning in the CrMnFeCoNi high-entropy alloy, Acta Mater. 118 (2016) 152–163, https://doi.org/10.1016/j.actamat.2016.07.038.
[38] F. Bahadur, K. Biswas, N.P. Gurao, Micro-mechanisms of microstructural damage due to low cycle fatigue in CoCuFeMnNi high entropy alloy, Int. J. Fatigue 130 (2020), 105258, https://doi.org/10.1016/j.ijfatigue.2019.105258.
[39] D. Lin, L. Xu, Y. Han, Y. Zhang, H. Jing, Intermetallics structure and mechanical properties of a FeCoCrNi high-entropy alloy fabricated via selective laser melting, Intermetallics 127 (2020), 106963, https://doi.org/10.1016/j.intermet.2020.106963.
[40] D. Lin, L. Xu, H. Jing, Y. Han, L. Zhao, F. Minami, Effects of annealing on the structure and mechanical properties of FeCoCrNi high-entropy alloy fabricated via selective laser melting, Addit. Manuf. 32 (2020), 101058, https://doi.org/10.1016/j.addma.2020.101058.
[41] Z. Wu, H. Bei, G.M. Pharr, E.P. George, Temperature dependence of the mechanical properties of equiatomic solid solution alloys with face-centered cubic crystal structures, Acta Mater. 81 (2014) 428–441, https://doi.org/, Acta Mater. 81 (2014) 428–441. https://doi.org/10.1016/j.actamat.2014.08.026.
[42] G.A. Salishchev, M.A. Tikhonovsky, D.G. Shaysultanov, N.D. Stepanov, A. V. Kuznetsov, I.V. Kolodiy, A.S. Tortika, O.N. Senkov, Effect of Mn and v on structure and mechanical properties of high-entropy alloys based on CoCrFeNi system, J. Alloy. Compd. 591 (2014) 11–24, https://doi.org/10.1016/j.jallcom.2013.12.210.
[43] J.J. Licavoli, M.C. Gao, J.S. Sears, P.D. Jablonski, J.A. Hawk, Microstructure and mechanical behavior of high-entropy alloys, J. Mater. Eng. Perform. 24 (2015) 3685–3698, https://doi.org/10.1007/s11665-015-1679-7.
[44] J. Li, W. Jia, J. Wang, H. Kou, D. Zhang, E. Beaugnon, Enhanced mechanical properties of a CoCrFeNi high entropy alloy by supercooling method, Mater. Des. 95 (2016) 183–187, https://doi.org/10.1016/j.matdes.2016.01.112.
[45] D. Gu, Y.-C. Hagedorn, W. Meiners, G. Meng, R.J.S. Batista, K. Wissenbach, R. Poprawe, Densification behavior, microstructure evolution, and wear performance of selective laser melting processed commercially pure titanium, Acta Mater. 60 (2012) 3849–3860, https://doi.org/10.1016/j.actamat.2012.04.006.
[46] S. Luo, P. Gao, H. Yu, J. Yang, Z. Wang, X. Zeng, Selective laser melting of an equiatomic AlCrCuFeNi high-entropy alloy: processability, non-equilibrium microstructure and mechanical behavior, J. Alloy. Compd. 771 (2019) 387–397, https://doi.org/10.1016/j.jallcom.2018.08.290.
[47] N.K. Tolochko, S.E. Mozzharov, I.A. Yadroitsev, T. Laoui, L. Froyen, V.I. Titov, M. B. Ignatiev, Balling processes during selective laser treatment of powders, Rapid Prototyp. J. 10 (2004) 78–87, https://doi.org/10.1108/13552540410526953.
[48] J.J. Marattukalam, D. Karlsson, V. Pacheco, P. Beran, U. Wiklund, U. Jansson, B. Hjörvarsson, M. Sahlberg, The effect of laser scanning strategies on texture, mechanical properties, and site-specific grain orientation in selective laser melted 316L SS, Mater. Des. 193 (2020), 108852, https://doi.org/10.1016/j.matdes.2020.108852.
[49] G.E. Lloyd, A.B. Farmer, D. Mainprice, Misorientation analysis and the formation and orientation of subgrain and grain boundaries, Tectonophysics 279 (1997) 55–78, https://doi.org/10.1016/S0040-1951(97)00115-7.

[50] K. Liu, M. Komarasamy, B. Gwalani, S. Shukla, R.S. Mishra, Fatigue behavior of ultrafine grained triplex Al0.3CoCrFeNi high entropy alloy, Scr. Mater. 158 (2019) 116–120, https://doi.org/10.1016/j.scriptamat.2018.08.048.
[51] I.V. Kireeva, Y.I. Chumlyakov, A.V. Vyrodova, Z.V. Pobedennaya, I. Karaman, Effect of twinning on the orientation dependence of mechanical behaviour and fracture in single crystals of the equiatomic CoCrFeMnNi high-entropy alloy at 77K, Mater. Sci. Eng. A 784 (2020), 139315, https://doi.org/10.1016/j.msea.2020.139315.
[52] F. Otto, A. Dlouhy, C. Somsen, H. Bei, G. Eggeler, E.P. George, The influences of temperature and microstructure on the tensile properties of a CoCrFeMnNi high-entropy alloy, Acta Mater. 61 (2013) 5743–5755, https://doi.org/10.1016/j.actamat.2013.06.018.
[53] M. Koyama, T. Sawaguchi, K. Tsuzaki, Deformation twinning behavior of twinning-induced plasticity steels with different carbon concentrations - part 2: proposal of dynamic-strain-aging-assisted deformation twinning, ISIJ Int 55 (2015) 1754–1761, https://doi.org/10.2355/isijinternational.ISIJINT-2015-070.
[54] K.M. Rahman, V.A. Vorontsov, D. Dye, The effect of grain size on the twin initiation stress in a TWIP steel, Acta Mater. 89 (2015) 247–257, https://doi.org/10.1016/j.actamat.2015.02.008.
[55] X.H. An, S.D. Wu, Z.G. Wang, Z.F. Zhang, Significance of stacking fault energy in bulk nanostructured materials: insights from Cu and its binary alloys as model systems, Prog. Mater. Sci. 101 (2019) 1–45, https://doi.org/10.1016/j.pmatsci.2018.11.001.
[56] H. Mughrabi, Dislocation wall and cell structures and long-range internal stresses in deformed metal crystals, Acta Met. 31 (1983) 1367–1379, https://doi.org/10.1016/0001-6160(83)90007-X.
[57] A. Piglione, B. Attard, V. Vieira Rielli, C.-T. Santos Maldonado, M.M. Attallah, S. Primig, M.-S. Pham, On the constitutive relationship between solidification cells and the fatigue behaviour of IN718 fabricated by laser powder bed fusion, Addit. Manuf. 47 (2021), 102347, https://doi.org/10.1016/j.addma.2021.102347.
[58] Z. Li, B. He, Q. Guo, Strengthening and hardening mechanisms of additively manufactured stainless steels: the role of cell sizes, Scr. Mater. 177 (2020) 17–21, https://doi.org/10.1016/j.scriptamat.2019.10.005.
[59] B. Chen, P.E.J. Flewitt, A.C.F. Cocks, D.J. Smith, A review of the changes of internal state related to high temperature creep of polycrystalline metals and alloys, Int. Mater. Rev. 60 (2015) 1–29, https://doi.org/10.1179/1743280414Y.0000000041.
[60] D. Hull, D.J. Bacon, Chapter 10 - Strength of Crystalline Solids, in: D. Hull, D.J.B. T.-I. to D. (Fifth E. Bacon (Eds.), Butterworth-Heinemann, Oxford, 2011: pp. 205–249. https://doi.org/https://doi.org/10.1016/B978-0-08-096672-4.00010–4.
[61] Z. Lei, X. Liu, Y. Wu, H. Wang, S. Jiang, S. Wang, X. Hui, Y. Wu, B. Gault, P. Kontis, D. Raabe, L. Gu, Q. Zhang, H. Chen, H. Wang, J. Liu, K. An, Q. Zeng, T.G. Nieh, Z. Lu, Enhanced strength and ductility in a high-entropy alloy via ordered oxygen complexes, Nature 563 (2018) 546–550, https://doi.org/10.1038/s41586-018-0685-y.
[62] X.H. An, Q.Y. Lin, S.D. Wu, Z.F. Zhang, Mechanically driven annealing twinning induced by cyclic deformation in nanocrystalline Cu, Scr. Mater. 68 (2013) 988–991, https://doi.org/10.1016/j.scriptamat.2013.02.053.
[63] P. Li, S.X. Li, Z.G. Wang, Z.F. Zhang, Unified factor controlling the dislocation evolution of fatigued face-centered cubic crystals, Acta Mater. 129 (2017) 98–111, https://doi.org/10.1016/j.actamat.2017.02.057.
[64] L. Cui, D. Deng, F. Jiang, R.L. Peng, T. Xin, R.T. Mousavian, Z. Yang, J. Moverare, Superior low cycle fatigue property from cell structures in additively manufactured 316L stainless steel, J. Mater. Sci. Technol. 111 (2022) 268–278, https://doi.org/10.1016/j.jmst.2021.10.006.
[65] H. Idrissi, K. Renard, L. Ryelandt, D. Schryvers, P.J. Jacques, On the mechanism of twin formation in Fe-Mn-C TWIP steels, Acta Mater. 58 (2010) 2464–2476, https://doi.org/10.1016/j.actamat.2009.12.032.
[66] Q. Zhu, L. Kong, H. Lu, Q. Huang, Y. Chen, Y. Liu, W. Yang, Z. Zhang, F. Sansoz, H. Zhou, J. Wang, Revealing extreme twin-boundary shear deformability, Met. Nanocryst. (2021) 1–10, https://doi.org/10.1126/sciadv.abe4758.
[67] S. Mahajan, G.Y. Chin, Formation of deformation twins in F.C.C. crystals, Acta Met. 21 (1973) 1353–1363, https://doi.org/10.1016/0001-6160(73)90085-0.
[68] S. Allain, J.P. Chateau, D. Dahmoun, O. Bouaziz, Modeling of mechanical twinning in a high manganese content austenitic steel, Mater. Sci. Eng. A 387–389 (2004) 272–276, https://doi.org/10.1016/j.msea.2004.05.038.
[69] G. Laplanche, A. Kostka, C. Reinhart, J. Hunfeld, G. Eggeler, E.P. George, Reasons for the superior mechanical properties of medium-entropy CrCoNi compared to high-entropy CrMnFeCoNi, Acta Mater. 128 (2017) 292–303, https://doi.org/10.1016/j.actamat.2017.02.036.
[70] J.P. Hirth, H.C.R. (Eds. R.E. Reed-Hill, J.P. Hirth, Deformation twinning, (1963) 112.
[71] H. Fujita, S. Ueda, Stacking faults and f.c.c. (γ) → h.c.p. (ϵ) transformation in 18 8-type stainless steel, Acta Met. 20 (1972) 759–767, https://doi.org/10.1016/0001-6160(72)90104-6.
[72] Q. Zhu, Q. Huang, Y. Tian, S. Zhao, Y. Chen, G. Cao, K. Song, Y. Zhou, W. Yang, Z. Zhang, X. An, H. Zhou, J. Wang, Hierarchical twinning governed by defective twin boundary in metallic materials, Sci. Adv. 8 ((2022), https://doi.org/10.1126/sciadv.abn8299.
[73] A.Y. Chen, L.L. Zhu, L.G. Sun, J.B. Liu, H.T. Wang, X.Y. Wang, J.H. Yang, J. Lu, Scale law of complex deformation transitions of nanotwins in stainless steel, Nat. Commun. 10 (2019) 1403, https://doi.org/10.1038/s41467-019-09360-1.
[74] P.Y. Chen, C. Lee, S.Y. Wang, M. Seifi, J.J. Lewandowski, K.A. Dahmen, H.L. Jia, X. Xie, B.L. Chen, J.W. Yeh, C.W. Tsai, T. Yuan, P.K. Liaw, Fatigue behavior of high-entropy alloys: a review, Sci. China Technol. Sci. 61 (2018) 168–178, https://doi.org/10.1007/s11431-017-9137-4.
[75] Z.J. Zhang, P. Zhang, L.L. Li, Z.F. Zhang, Fatigue cracking at twin boundaries: effects of crystallographic orientation and stacking fault energy, Acta Mater. 60 (2012) 3113–3127, https://doi.org/10.1016/j.actamat.2012.02.016.
[76] Y. Liu, J. Zhou, The fatigue crack growth in hierarchically nano-twinned materials, Eng. Fract. Mech. 204 (2018) 63–71, https://doi.org/10.1016/j.engfracmech.2018.10.012.
[77] Y. Wei, Y. Li, L. Zhu, Y. Liu, X. Lei, G. Wang, Y. Wu, Z. Mi, J. Liu, H. Wang, H. Gao, Evading the strength-ductility trade-off dilemma in steel through gradient hierarchical nanotwins, Nat. Commun. 5 (2014) 1–8, https://doi.org/10.1038/ncomms4580.
[78] A.M. Wang, J. Liu, J. Zhao, H.M. Zhang, Z.S. Cui, Effect of pre-deformation on twins evolution and mechanical properties for AZ80 magnesium alloy, Suxing Gongcheng Xuebao/J. Plast. Eng. 28 (2021) 124–130, https://doi.org/10.3969/j.issn.1007-2012.2021.11.017.
[79] P. Zhou, Z.Y. Liang, R.D. Liu, M.X. Huang, Evolution of dislocations and twins in a strong and ductile nanotwinned steel, Acta Mater. 111 (2016) 96–107, https://doi.org/10.1016/j.actamat.2016.03.057.